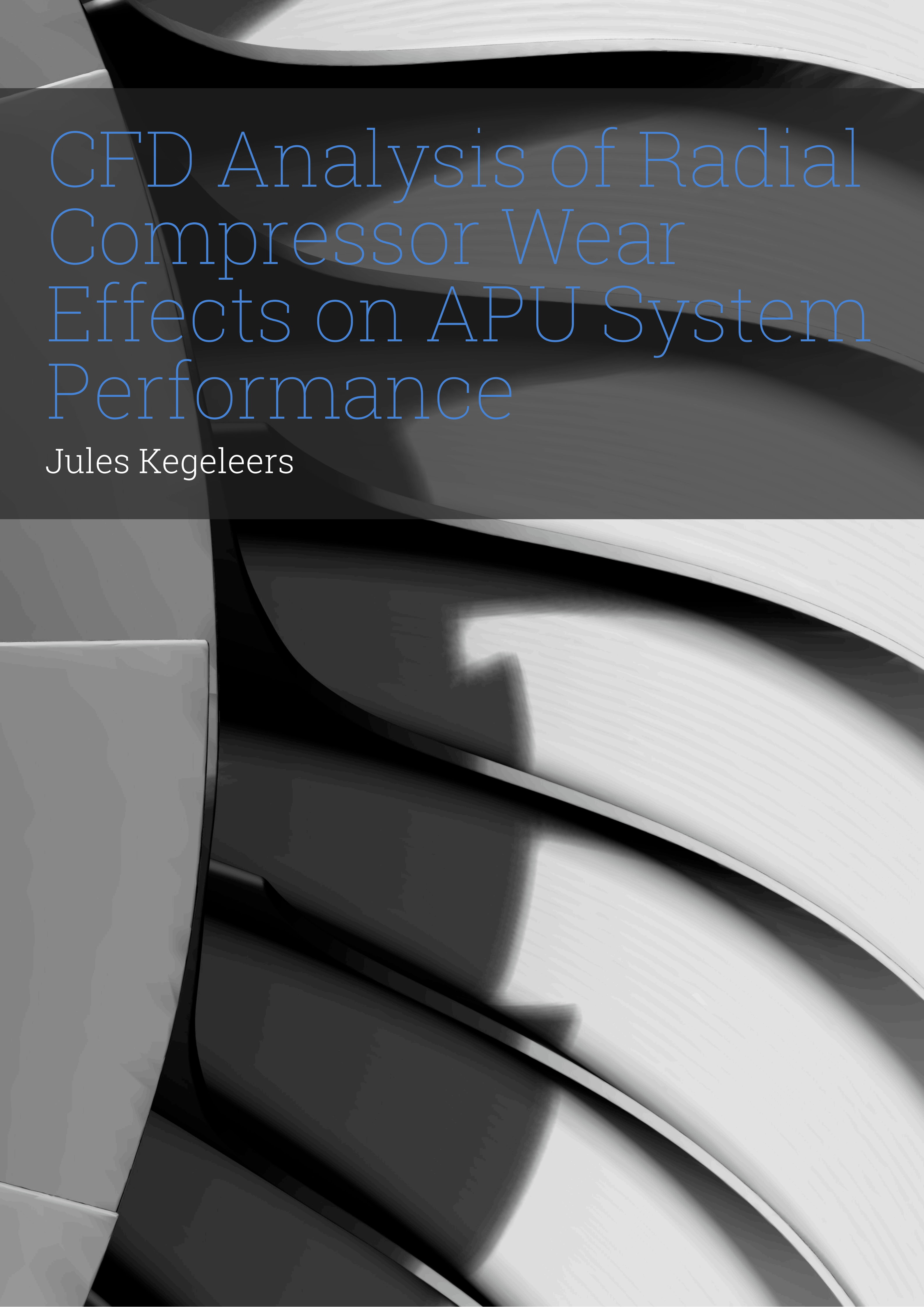

CFD Analysis of Radial Compressor Wear Effects on APU System Performance

Jules Kegeleers

CFD Analysis of Radial Compressor Wear Effects on APU System Performance

by

Jules Kegeleers

Master of Science Thesis
Aerospace Engineering

Student number:	5488192	
Thesis committee:	Dr. W.P.J. Visser	TU Delft, Supervisor
	O. Kogenhop MSc.	EPCOR
	Dr.ir. M. Pini	TU Delft, Chair
	Dr.ir. A.H. van Zuijlen	TU Delft

Abstract

Auxiliary Power Units (APUs) are critical for the safe and reliable operation of modern aircraft, providing electrical power and compressed air during ground operations and in-flight emergencies. As APUs operate worldwide, they are exposed to harsh conditions such as sand ingestion leading to compressor deterioration and APU performance degradation. The objective of this thesis, conducted in collaboration with EPCOR, was to investigate whether Computational Fluid Dynamics (CFD) can be used to predict compressor performance degradation and its impact on overall APU performance to improve APU condition monitoring and predictive maintenance strategies.

In this study, the centrifugal compressor of a Pratt & Whitney APS5000, as used in the Boeing 787, was reverse engineered using 3D scans of the impeller and diffuser. These geometries were reconstructed and implemented in a CFD model that was validated against a pass-off test measurement. Through a literature study, it was concluded that the main compressor deterioration effects are increases in impeller tip clearance and impeller and diffuser surface roughness. The impact of these effects on compressor efficiency, pressure ratio, and flow capacity was simulated and incorporated into a Gas turbine Simulation Program (GSP) model to assess the resulting APU performance degradation by evaluating changes in Exhaust Gas Temperature (EGT), fuel flow, and compressor pressure ratio.

The results show that increased surface roughness and tip clearance both lead to reductions in compressor efficiency, pressure ratio and flow capacity, which translate into higher exhaust gas temperatures and increased fuel flow at the APU system level. Plotting the reduction in pressure ratio, increase in EGT and increase in fuel flow as a function of compressor efficiency deterioration and flow capacity deterioration, a compressor deterioration map was made. This map is overlaid with simulated points of varying surface roughness and/or tip clearance serving as a decision tool to aid in root cause determination during APU disassembly.

Although the absolute accuracy of the results is limited by assumptions in geometry reconstruction, turbulence modeling, and validation data, the study provides an indication of the relative reduction in APU system performance and demonstrates a working proof of concept in the form of a deterioration map. Therefore, it is concluded that compressor CFD with gas turbine simulation offers a viable approach to assess compressor deterioration effects and their impact on APU performance, thus enhancing APU condition monitoring and supporting root cause determination in a maintenance environment.

Acknowledgement

This thesis was made possible with the support of EPCOR and its technicians, whom I would like to thank for their practical assistance, expertise, and willingness to share their experience, as well as my supervisors, Dr. W.P.J. Visser and O. Kogenhop, for their guidance and support.

Contents

List of Figures

List of Tables

Nomenclature

Abbreviations

Abbreviation	Definition
AFR	Air-Fuel Ratio
APU	Auxiliary Power Unit
CAD	Computer-Aided Design
CFD	Computational Fluid Dynamics
DES	Detached Eddy Simulation
DNS	Direct Numerical Simulation
EGT	Exhaust Gas Temperature
FOD	Foreign Object Damage
ISA	International Standard Atmosphere
LES	Large Eddy Simulation
RANS	Reynolds-Averaged Navier-Stokes
Realizable $k-\epsilon$	Realizable k-epsilon turbulence model
RMS	Root Mean Square
RNG $k-\epsilon$	Re-Normalization Group k-epsilon turbulence model
RSM	Reynolds Stress Models
SA	Spalart–Allmaras turbulence model
SFC	Specific Fuel Consumption
SST $k-\omega$	Shear Stress Transport k-omega turbulence model
TC	Tip Clearance
$k-\epsilon$	Standard k-epsilon turbulence model
$k-\omega$	Standard k-omega turbulence model

Symbols

Symbol	Definition	Unit
C_p	Specific heat capacity at constant pressure	$[\mathrm{J/(kg\,K)}]$
$dEGT$	Relative difference in exhaust gas temperature	[K]
dW_f	Relative difference in fuel flow	[%]
$d\dot{m}_{corr}$	Relative difference in flow capacity	[%]
$d\eta_c$	Relative difference in isentropic compressor efficiency	[%]
h	Total enthalpy	[J/kg]
k_s	Sand grain roughness	[μm]
L	Characteristic length	[m]
LHV	Lower heating value	[J/kg]
$\dot{m}_{corr}$	Corrected mass flow rate	[kg/s]
N_c	Corrected (non-dimensional) rotor speed	[-]
n	Rotor speed	[rpm]
P_s	Shaft power	[W]
P_t	Total pressure	[Pa]
PF	Power factor	[-]
p_{ref}	Reference pressure	[Pa]
R_a	Average surface roughness	[μm]
R_{rms}	Root mean square surface roughness	[μm]

Symbol	Definition	Unit
Re	Reynolds number	[-]
S	Apparent power	$[\mathrm{kV\,A}]$
T_{ref}	Reference temperature	$[\mathrm{K}]$
T_t	Total temperature	$[\mathrm{K}]$
u	Characteristic velocity	$[\mathrm{m/s}]$
u_τ	Friction velocity at wall	$[\mathrm{m/s}]$
W	Mass flow rate	$[\mathrm{kg/s}]$
w_{actual}	Actual specific work	$[\mathrm{J/kg}]$
y	Wall normal distance	$[\mathrm{m}]$
y^+	Dimensionless wall distance	[-]
δ	Inlet pressure divided by reference pressure	[-]
$d\pi_{tt}$	Relative difference in total-to-total pressure ratio	$[\%]$
η_c	Isentropic compressor efficiency	$[\%]$
η_{gen}	Generator efficiency	$[\%]$
γ	Specific heat ratio	[-]
μ	Dynamic viscosity	$[\mathrm{N\,s/m^2}]$
ν	Kinematic viscosity	$[\mathrm{m^2/s}]$
π_{tt}	Total-to-total pressure ratio	[-]
ρ	Fluid density	$[\mathrm{kg/m^3}]$
θ	Inlet temperature divided by reference temperature	[-]

1

Introduction

Auxiliary Power Units or APUs as used in commercial aviation are turboshaft engines often located in the tail cone of an airplane. They play a vital role in commercial aviation by providing electrical power and compressed air to various aircraft systems during ground operations and in-flight emergencies during main engine failure. Since they are a safety critical component, they need to be maintained regularly to ensure reliability.

This study is conducted in collaboration with EPCOR who maintain and overhaul APUs and pneumatic components for a number of airlines. By monitoring APU performance indicators like exhaust gas temperature and number of cycles, the company advices airlines when the APU is in need of maintenance. As these APUs operate all over the world they are subjected to harsh environments like sand and oil ingestion, ice formation or bird strikes. In Eastern countries, EPCOR has seen APUs that need to be overhauled 50% faster compared to other climates as a result of sand and dust ingestion. Since the APU compressor is the first component in the APU gas path, these environments can cause compressor erosion and fouling, deteriorating the compressor stage and reducing the overall APU efficiency by increasing the needed Exhaust Gas Temperature or EGT and specific fuel consumption.

The research objective of this study is to investigate APU performance degradation as a result of compressor performance deterioration to improve APU predictive maintenance strategies. Components of an existing relevant compressor from a Boeing 787 airliner are reverse engineered using 3D scans to construct a Computational Fluid Dynamics or CFD model. By taking scans and measurements of both used and unused compressor components, compressor damage effects are modeled and simulated quantifying the performance degradation of the compressor. Using a Gas turbine Simulation Program or GSP the APU system performance degradation as a result of this compressor deterioration can then be simulated and quantified to aid APU condition monitoring and maintenance planning.

This thesis is structured as follows. Section 2 provides the relevant research objective and sub-questions this study hopes to answer. Section 3 contains a literature study to investigate compressor deterioration mechanisms with the relevant damage effects, CFD turbulence models and reverse engineering strategies. Section 4 includes the compressor reverse engineering process and CFD model setup and development. This is followed up by Section 5 where the results are presented and analyzed. Section 6 reflects on the study and discusses possible implications or limitations. Finally, section 7 summarizes the main findings and gives recommendations for further research.

2

Research Objective

This thesis concerns simulation of APU performance degradation through centrifugal compressor performance deterioration. The goal of the paper is to use computational fluid dynamics to predict compressor performance deterioration as a result of compressor wear. As the APU compressor geometries are not available they need to be reverse engineered based on 3D scans of the real parts. Using this compressor performance deterioration, the overall APU performance loss and increased fuel consumption can be modeled with the goal of improving APU condition monitoring.

Main Research Question:
Can APU performance degradation as a result of compressor deterioration be estimated using compressor CFD simulation with reverse engineered compressor geometries?

Sub-questions:

- How can the impeller and diffuser geometry of a centrifugal compressor be reverse engineered to be used in CFD simulation?
- What are the main deterioration mechanisms in an APU centrifugal compressor and what are the corresponding damage effects?
- How can these damage effects and resulting performance loss be simulated in CFD simulations?
- Can the compressor CFD simulation with reverse engineered geometries be validated using an APU test cell result?
- Can the performance reduction of an APU with a degraded compressor be simulated?

3

Literature Study

3.1. Auxiliary power units in aircraft

An auxiliary power unit or APU originates from the first world war where a small internal combustion engine was used on military ships and airplanes to power critical systems when encountering a loss of power through main engine failure. This allows operation of communication equipment or restarting of the main engines. With the rise of the first military turbojet engines, APU's were used as they are crucial to restart the engine in case of engine failure. An example of this is the BMW 003 turbojet that used a two stroke two cylinder internal combustion engine to directly spin the compressor shaft of the turbojet during the starting procedure [1].

Current APU's are gas turbine turboshaft engines with the first being introduced in the Boeing 727 in 1963. It was located in the main landing gear bay of the aircraft allowing the aircraft to operate on smaller airports where ground power might not be available [2]. As the Boeing 727 has 3 main engines, the APU was not needed for extra redundancy and did not allow airborne operation [3]. Nowadays, most modern airliners include an APU that is located in the rear tail section of the aircraft with the exhaust pointing out of the tail cone. Although most modern airports provide ground power and even preconditioned air for cabin temperature control, the APU is still required to start one or both main engines using bleed air, and it also serves as an emergency power source in the event of a main engine failure during flight [4].

When one of the main engines on an airliner fails the APU can be switched on to restore full electrical power and provide bleed air if needed. In a scenario where both main engines fail, the APU allows restarting of the main engines, cabin pressurization and air condition through bleed air that is taken from a compressor stage or from a designated load compressor [4]. On a Boeing 777 the APU generator has the same output as the generator from a main engine allowing it run all essential loads of the aircraft. This includes electric hydraulic pumps enabling all power control units and control surfaces allowing full control over the airplane including high-lift devices, landing gear and brakes. It can thus be said that the redundancy of the APU plays a crucial role in aviation safety.

3.2. Auxiliary power units (APU) System and components

Commercial airliners use many different models and sizes of APU's with the size and power requirements varying depending on the application. Generally, an airliner APU consists of a turboshaft engine with 1-2 centrifugal compressor stages and 1-3 axial turbine stages on a common rotor shaft. Pneumatic power is provided through a load compressor or by extracting bleed air from the compressor stage. At the front of the engine a gearbox is attached to the rotor shaft and spins a generator to provide electrical power as well as accessories like the auxiliary starter generators, oil pumps, scavenge pumps, etc...

3.2.1. Boeing 787 APU (APS5000)

In this study, a Pratt & Whitney APS5000 as used in the Boeing 787 is investigated. As this airplane is all electric the APU layout is simpler than most as it does not provide bleed air.

A cross section of the APU is shown in Figure 3.1. It can be seen that air is drawn from an inlet plenum that is fed through a FOD or foreign object damage screen into a single stage centrifugal compressor. This compressed air is guided to a reverse flow annular combustion chamber where fuel is injected using swirlers around the circumference of the combustion chamber resulting in an air fuel mixture enabling a continuous cycle when the engine is running. Of course, on startup the mixture needs to be ignited by igniters. After the combustion chamber the hot combustion gasses spin a dual stage axial turbine which spins the common rotor shaft. At the front of the power unit, a gearbox driven by the rotor shaft reduces the rotational speed and drives 2 auxiliary starter generators that are used to start the power unit and supply a combined $450\,\mathrm{kVA}$ at nominal speed. As the generators are able to operate at varying frequencies, the rotational speed of the APU can be increased at flying altitudes.

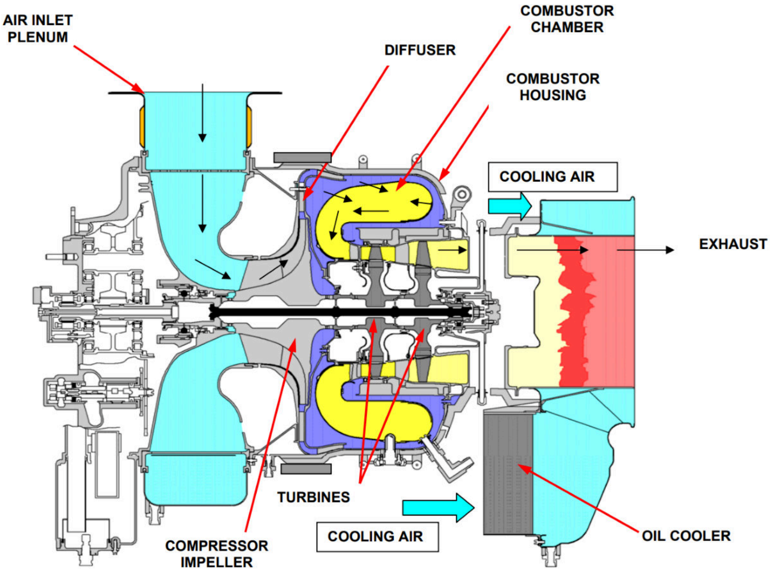

Figure 3.1: APS5000 APU cross section.

3.2.2. APS5000 Compressor

As the APU does not provide bleed air, it does not have a load compressor eliminating the need for a surge control valve and inlet guide vane. The centrifugal stage contains three blade rows consisting of an impeller as shown in Figure 3.2 and a vaned diffuser with an outlet guide vane which is shown in Figure 3.3. Because of the impeller diameter and high operational speed of the compressor, the impeller operates in the transonic regime. Turboshaft engines in helicopters and APU's are trending towards higher power to weight ratio and reduced Specific Fuel Consumption or SFC [5]. By reducing the amount of stages the overall weight and size is reduced resulting in the in the compressor staged needing a high per stage pressure ratio.

3.3. APU Compressor Deterioration

Performance degradation in gas turbines is becoming an increasingly important topic with [6] showing an increase in the number of published degradation related journal articles. Both external influences and general running can cause wear reducing the overall performance of the machine. External influences like dust and sand ingestion [7, 8], ice formation and ingestion [9], volcanic ash, fly ash from coal plants [10], bird strikes or oil and fuel leaks can all adversely affect machine performance resulting in increased exhaust gas temperature or EGT, increased SFC or unreliable operation. This section of the study will first discuss the various compressor deterioration mechanisms after which the performance impact of the main damage effects is discussed.

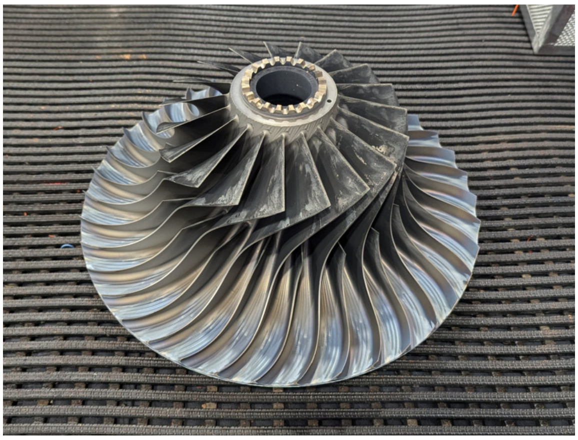

Figure 3.2: Compressor impeller.

Figure 3.3: Compressor diffuser with exit guide vanes.

3.3.1. Deterioration mechanism

Particle ingestion and erosion

Through military applications it was found that turboshaft engines as used in helicopters are found to have a reduced lifespan when operating in sandy areas [11]. Erosion is caused by ingestion of abrasive particles removing material from flow surfaces resulting in reduced output power, increased SFC and decreased surge margin [12, 13]. Sources [13, 14, 15] all investigate ways of determining where this erosion in rotating cascades will occur in order to better protect gas turbine engines.

Similar to the aforementioned helicopter engines, APU's are operated all over the world thus subjecting them to particle ingestion like sand and dust when operating in sandy areas. Ingestion of solid particles in rotating cascades can lead to both structural and aerodynamic performance deterioration as discussed in [16]. The source indicates that two-phase flow conditions as a result of particle ingestion can lead to a change in blade surface pressure distribution altering the engine performance during the period of ingestion. Particle ingestion can also cause erosion damage increasing the surface roughness, pitting and cutting the blade resulting in an increased total pressure loss across the compressor blade row.

Source [17] reports an experimental test where the intake of an axial flow compressor was injected with sand during operation. The results show a reduced stage efficiency from $1.86\,\%$ up to $2.89\,\%$ at higher mass flow rate with the main cause being increased losses at the blade leading edge tip. The blade loading was found to be very similar up to a radius of 0.9 blade length with a $5.5\,\%$ decrease in blade loading at the tip section. The main contributors to the loss in stage efficiency are said to be: changes in blade leading and trailing edge, surface roughness, tip leakage as a result of tip clearance and pressure distribution. Although the tested machine is an axial compressor, it can be assumed that a centrifugal compressor will suffer similar types of wear.

Not only small particles but larger foreign objects can also be ingested. Like most APU's, the APS5000 has an air inlet screen to prevent ingestion of FOD objects during operation. During APU disassembly, EPCOR technicians often find remains of birds stuck to this air inlet screen with parts of the bird being sucked through the compressor. The holes in the inlet screen are sizable so small rocks and other debris can still pass through, possibly chipping or breaking off pieces of blades. An example of impeller leading edge chipping is shown in Figure 3.4.

Figure 3.5 shows the same impeller with a deformed blade resulting from the APU starting while the impeller was frozen solid. Ice can form in cold climates after ingesting water or as a result of condensation. Although this is not a common occurrence, APU's generally do not have any de-icing systems possibly resulting in significant damage as is the case in this example.

Figure 3.4: Impeller leading edge blade chipping and fouling.

Figure 3.5: Impeller blade deformation marked by red circle.

Another observation from the ECPOR technicians is the reduced lifespan of APU's operating in sandy areas as a result of cooling passages clogging up. This results in reduced cooling with parts of the APU running at hotter temperatures. A common outcome of this is overheating of the turbine blades leading to the blades deforming or ”walking” potentially seizing the APU. A similar investigation is discussed in [18]. As this is not related to the compressor section of the APU, it is not investigated further.

Rubbing

Rubbing is another damage mechanism that is often seen by EPCOR technicians. The impeller touches the shroud during operation causing abrasion which removes material on the impeller and grooves the shroud. Figure 3.6 shows a worn impeller tip with Figure 3.7 showing a part of the corresponding shroud damage. EPCOR technicians mostly attribute rubbing to vibrations, bearing wear or foreign object damage changing the shape of an impeller blade. Damage is said to mostly occur at mid span of the impeller tip or on the impeller outlet. As shown in Figure 3.7, the damage on the shroud is usually in local regions and not on the full circumference as is the case on the impeller. As can be expected, rubbing can increase the tip clearance as material is removed from the impeller tip [12]. Increased surface roughness on the damaged regions of shroud can also be expected.

Figure 3.6: Impeller blade rubbing damage.

Figure 3.7: Shroud rubbing damage.

Fouling

Another consequence of airborne contaminants is compressor fouling. Previously discussed abrasive contaminants but also non-abrasive contaminants like oil and combustion products like hydrocarbons can accumulate on the surfaces of the compressor stage [10]. Fouling increases surface roughness and can to a smaller degree change the shape of the flow surfaces [12]. Source [19] estimates gas turbine fouling in axial machines to be responsible for $70\,\%$ to $85\,\%$ of all gas turbine performance losses. Fouling also influences the operating characteristics of the gas turbine as the reduced mass flow results in the stage operating closer to the surge line thus reducing the available surge margin [10, 20]. Figure 3.4 shows fouling with a visible texture at the leading edge of the blade. In Figure 3.5 a clear color difference between the pressure and suction side as well the blades and hub as a result of impeller fouling can be seen.

As discussed in [21], both online and offline washing of a gas turbine compressor can slow down or reduce the amount of fouling a compressor experiences and recover up to $30\,\%$ of the lost power in certain scenarios. Reference [22] investigated the economic viability of online compressor washing for a variety of gas turbine compressors and concluded that higher washing intervals increased return on investment in most cases. In auxiliary power units like the APS5000, washing is not on the maintenance schedule. This is likely because they are difficult to access and having a shorter maintenance interval would result in increased downtime for airlines.

3.3.2. Performance degradation

Through the degradation mechanisms it is concluded that airborne contaminants can result in both compressor erosion and fouling while bearing wear and vibrations can cause compressor rubbing. Similar to source [12], the main damage effects are concluded to be increased surface roughness and increased tip clearance. As the goal of this study is to investigate the possibility of simulating performance degradation of a centrifugal compressor through CFD simulations, the performance degradation as a result of tip clearance and surface roughness is investigated further.

Tip Clearance effects

In a centrifugal compressor, a tip clearance is needed to avoid the impeller hitting the shroud as thermal expansion and blade deformation change the impeller shape during operation. As discussed in [23], investigating the effect of tip clearance on compressor performance is difficult because the effect can not be isolated as other loss mechanisms will also be present. Measuring the clearance on a running impeller also posses problems as this gap is small and only a fraction of the blade height. Measuring the cold clearance before running is inaccurate as thermal expansion and impeller thrust forces during operation change the actual clearance. It is also discussed that the tip clearance is often not circumferentially uniform because of machining tolerances. Source [24] conducted an aero-thermo-mechanical analyses for 2 different impellers and concluded a reduction of $25.4\,\%$ and $46.7\,\%$ in tip clearance at the leading edge of the blade as a result of impeller deformation. The cold tip clearance therefore changes to a non-uniform tip clearance during operation.

This tip clearance results in a leakage flow or tip leakage where fluid escapes between the impeller tip and shroud of the compressor moving from the pressure to the suction of the blade. Tip clearance loss is extensively researched with many sources creating relations to try and model the loss [25, 26, 27, 28]. Reference [23] indicates the leaking fluid not only causes a pressure loss but it can also disturb the flow structure in the next blade channel as it enters the channel in the opposite direction to the shroud secondary flow direction. This can result in a wake which interferes with the primary flow. The parameters of the impeller geometry, diffuser geometry and the tip clearance can all influence the primary and secondary flows making it difficult to evaluate the flow field and losses for a single parameter resulting in many sources reporting the overall performance difference of the compressor when changing tip clearance [29].

To allow for an equal comparison independent of the geometry, sources investigating tip clearance in compressors mostly use clearance ratio which is the tip clearance divided by the blade height of the impeller at the outlet. Source [27] investigated the deterioration of compressor performance due to tip clearance and concluded that performance is always reduced with increased tip clearance. For an equal clearance ratio, compressors with a higher pressure ratio show reduced efficiency loss with reduced shaft speed or flow rate also reducing the performance loss. Reference [23] conducted an experimental test on an unshrouded centrifugal impeller where the running tip clearance was measured using a non brittle material on 3 places around the impeller resulting in a circumferential averaged measurement. After changing the axial tip clearance 3 times using shims, it was concluded that a single point increase in clearance ratio results in a $0.77\,\%$ reduction of pressure ratio with a $0.31\,\%$ loss in polytropic efficiency. A higher performance sensitivity is also observed at smaller clearances.

The effect of tip clearance on an centrifugal compressor as used in an APU is investigated in [30]. The axial tip clearance is varied 7 times after which it is concluded that a single point change in tip clearance results in a reduction in isentropic efficiency ranging from $0.35\,\%$ to $0.45\,\%$. As expected, the pressure ratio also reduces. Interestingly, when the clearance increases, the surge line of the compressor occurs at higher mass flows thus narrowing the operating range while the choke line is almost unaffected. Reference [28] indicates that tip clearance ratio is almost proportional to efficiency drop and tip clearance loss. It is also concluded that the tip clearance ratio is the most influential factor on tip clearance loss although, not the only one. Sources [24] and [29] include many similar sources investigating compressor performance change as a result of tip clearance.

As expected, it can thus be concluded that the tip clearance is directly linked to the compressor efficiency and pressure ratio. Because of the complexity of the problem and the amount of influential parameters, a single relation to approximate the performance change as a result of increased tip clearance can not be made. It is however clear that an increase in tip clearance should result in a decrease in both isentropic efficiency and pressure ratio.

Regarding the APS5000 compressor, the cold tip clearance during assembly should be within a $0.09\,\mathrm{mm}$ window. Within EPCOR, this is measured with a feeler gauge at the impeller outlet on multiple different points around the circumference. Because of vibrations, bearing wear, thermal expansion and component deformation, it is difficult to estimate the running tip clearance of the impeller. Another point of difficulty is the measured cold tip clearance which often reduces instead of increasing. When measuring the cold tip clearance during disassembly as done during assembly, the tip clearance at the outlet of the impeller can decrease as was the case with the two APS5000 impellers that were shown in Figures 3.4 and 3.6. An EPCOR engineer mentioned that this is likely due to thrust bearing wear resulting in the common shaft moving axially thus reducing impeller tip clearance compared to the shroud.

To quantify the tip clearance as a result of wear on the impeller, a 3D scan of a used impeller is taken after which it is compared with the scan of a new unused impeller. It is then possible to see the deviation in vane contour as shown in Figure 3.8. This only quantifies the wear on the impeller mostly resulting from rubbing and does not include the aforementioned tip clearance reduction as a result of bearing wear etc. Impellers with severe rubbing damage are not scanned as they cannot be reused. The most severe rubbing case for an APS5000 compressor that was scanned is shown in Figure 3.9 and shows a maximum reduction of $0.27\,\mathrm{mm}$.

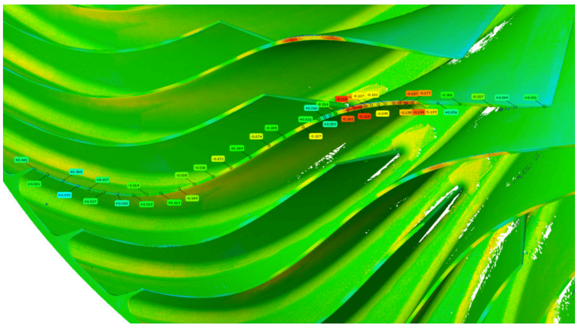

Figure 3.8: 3D scanned vane contour comparison of used and unused impeller.

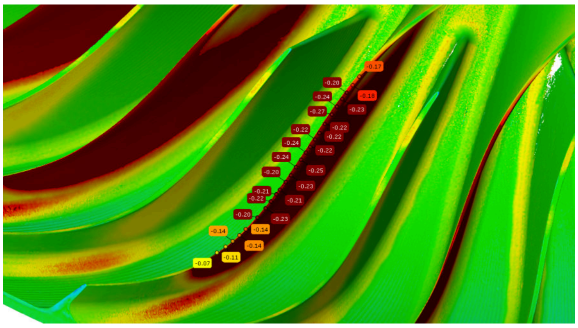

Figure 3.9: 3D scanned vane contour comparison of impeller with rubbing.

Surface Roughness effects

Increased surface roughness in gas turbines can occur as a result of erosion, corrosion or fouling and can influence fluid dynamics and heat transfer by affecting the boundary layer flow and turbulent structure [31]. In centrifugal compressors, roughness influences compressor loss through earlier flow transition, increased boundary layer losses, and flow separation as is the case in axial compressors [6]. Sources [32, 33, 34] investigated the effect of roughness in centrifugal compressors using one-dimensional models and concluded that the effect of roughness increases with increasing Reynolds number [6].

Source [35] investigates roughness in a transonic axial compressor rotor and concludes that comparing a coating with a rough surface finish of $2.54 - 3.18\,\mu\text{m}$ with a smooth coating resulted in a $5\,\%$ loss in pressure ratio and a $3 - 5\,\%$ reduction in efficiency for an operating point near design mass flow. Performance deterioration modeling including validation with test results on an axial compressor is discussed in [36]. At both $90\,\%$ and $100\,\%$ speed the loss in pressure ratio reaches up to $0.5\,\%$ at high mass flow when a moderate average surface roughness or R_a of $4\,\mu\text{m}$ is considered. A larger effect is seen on the adiabatic efficiency which reduces by roughly $2\,\%$. Adding increased tip clearance to the model resulted in an additional $1.5\,\%$ to $2\,\%$ reduction in adiabatic efficiency.

Reference [37] investigated the possibility of predicting surface roughness effects on centrifugal compressor performance through a sand blasting experiment and corresponding CFD simulation. It was concluded that the FLUENT CFD solver underestimated the performance loss as a result of increased surface roughness. After increasing the surface roughness to align the CFD simulation with the test results it was found that the reduction in efficiency is almost linear with increased surface roughness. When increasing the surface roughness of only the impeller and diffuser surfaces the efficiency reduction was found to be in the order of $1\,\%$ per $4\,\mu\text{m}$ increase in R_a. When including the casing shroud the efficiency reduction increased to $1.5\,\%$ per $4\,\mu\text{m}$ of increase in R_a

3.4. Turbomachinery CFD

Development of turbofan and turbojet engines is extremely expensive with the GE90 developed by General Electric in the 90's reported to have cost $1.6 Billion [38]. Because of these high development, testing and manufacturing costs, computational fluid dynamics or CFD plays a crucial role in predicting behavior of turbomachinery gas flow and machine performance with the design process almost completely relying on it [39, 40].

As said in [41], global parameters like pressure ratio and efficiency can be predicted with reasonable accuracy. Accurately simulating flow fields including unsteady effects and transient behavior is much more difficult. For the scope of this project it is not necessary to accurately capture these flow physics but it is of importance to accurately simulate the performance characteristics of the APU compressor depending on the geometry and relevant damage metrics of the impeller. The goal is to achieve this by simplifying the simulation as much as possible while maintaining accuracy.

3.4.1. Modeling & Simulation Tools

Many different CFD tools exist for different applications. Open source software like OpenFoam and SU2 are flexible but can be harder to learn as they are operated using a command line interface. Ansys Fluent and STAR-CCM+ are widely used in industry because of their easy of use and robustness. In terms of Turbomachinery specific tools, Ansys CFX is the most widely used and has a large amount of available documentation. It also allows for simple integration from geometry to meshing to simulation. Most available publications and sources like [41] also used CFX allowing for comparison.

3.4.2. Turbulence modeling

Flow in turbomachinery is inherently turbulent having a high Reynolds number. Simulating this turbulence correctly is important to accurately simulate the flow and predict the performance of the machine. Directly solving the Navier-Stokes equations for all turbulence length and time scales requires a large amount of computational power as the number of needed grid points increases exponentially with the Reynolds number. Source [42] indicates that the number of required grid points N is proportional to $Re^{9/4}$ with later source [43] reporting a number of grid points ${Re_{Lx}}^{37/14}$. As indicated in [44], Direct Numerical Simulation or DNS is currently out of reach for most flows with high Reynolds numbers because of the high computational cost.

Turbulent flow consists of eddies with different sizes and amounts of energy. The smaller the eddy, the finer the mesh needs to be to resolve them. By decomposing the turbulent flow into larger eddies that are resolved by the mesh and smaller eddies that are modeled by a Sub-Grid model, the needed mesh size and computational power is reduced. This is called a Large Eddy Simulation or LES. Although the needed CPU power is reduced, LES for high Reynolds number flow is still demanding and generally restricted to academia [44].

In turbomachinery industry, Reynolds-Averaged Navier-Stokes or RANS is the most used turbulence model [45]. By time averaging the Navier-Stokes equations a mean flow is obtained. This turbulence model is thus an approximation that averages the fluctuating quantities of the turbulence solving none of the turbulence eddies and greatly reducing the needed computational power. As a result of this averaging, transient or unsteady behavior can not be accurately captured using RANS models unlike LES and DNS where both unsteady behavior and transient flow can be simulated. As said in [45], ”Reynolds-averaged Navier–Stokes numerical simulations solvers, although they are affected by numerical and physical approximations, perform reasonably accurately and require less computational resources”. Because of these approximations, these models need to be used correctly and in the right conditions as it is known that RANS simulations can perform poorly outside of steady state or in off-design conditions. Reference [46] concludes that compressor performance and related flow fields are predicted with reasonable accuracy when performed close to design condition. Despite turbulence methods like hybrid LES-RANS or DES becoming more popular, RANS is the current most used turbulence model and should allow accurate simulation of the overall machine performance while greatly reducing the needed computational power.

3.4.3. RANS Turbulence models

RANS turbulence models rely on decomposing the turbulent flow into a mean or time averaged flow field and a fluctuating flow field. Substituting this decomposition into the Navier-Stokes equations and performing an averaging process results in simplified equations for the mean flow. A result of this averaging process is a Reynolds-stress term sometimes called the Reynolds stress tensor. To close and solve the RANS equations this term needs to be modeled resulting in a variation of RANS turbulence models.

As the RANS turbulence models have been in use for a long time there is a large amount and wide variety of models. The most commonly used class are the eddy viscosity models consisting of the following most widely used models:

- $k-\epsilon$ is one of the first turbulence models and widely used. It consists of two equations which are a partial differential equation for the turbulent kinetic energy k and a transport equation for the turbulence dissipation rate ϵ. Multiple versions of this model like the RNG $k-\epsilon$ and Realizable $k-\epsilon$ models try to make up certain shortcomings of the model. A known drawback is that it is not accurate at predicting boundary layers with adverse pressure gradients [47]. All the following models were proposed at a similar time and aim to improve this behavior.
- Spalart-Allmaras or SA is a one equation model that solves a transport equation for a modified turbulent viscosity originally proposed in source [48]. Because of this single transport equation less computational power is required. It performs well in simple attached flows but is known to be less suitable for turbomachinery applications as it shows premature stall prediction, predicts larger separation zones and increased total pressure loss [49].
- The Standard $k-\omega$ model is similar to the $k-\epsilon$ model but a transport equation for the specific turbulence dissipation rate ω is used instead of ϵ. The model is known to perform well near the wall even with adverse pressure gradients. The main drawback of the model is a high sensitivity in skin friction coefficient for small differences in free stream turbulence resulting in poor performance away from the wall [50].
- As the $k-\epsilon$ model does not have this problem a model combining the $k-\epsilon$ away from the wall with the $k-\omega$ model near the wall was proposed. This is called the Shear Stress Transport or SST $k-\omega$ model and is the most widely used model in industrial applications [51]. Figure 3.10 shows how the models are used depending on their distance from the wall. The blending region consists of blending functions where both models are used with a certain weight depending on the distance from the wall and local flow properties [52].

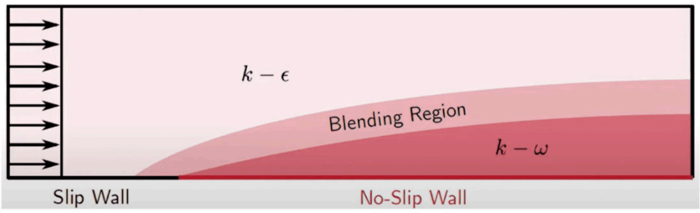

Figure 3.10: SST turbulence model blending [50].

Another category of RANS turbulence models are Reynolds Stress Models or RSM but they are not considered as they have a higher computational cost and are more prone to numerical instability [51]. It is thus concluded that the SST $k-\omega$ turbulence model is the best fit for the posed problem as it is the most used model in both turbomachinery and industrial applications as well as being the recommended model in the Ansys CFD RANS turbulence guide [47].

3.4.4. Meshing

Depending on the meshing software used, certain mesh statistics are generated to describe the mesh quality. These are used to ensure the mesh is of adequate quality when changing the mesh settings. As an example, the generated mesh statistics from Ansys TurboGrid are considered. The reported mesh statistics in order of importance as per TurboGrid documentation [53] are as follows:

1. Minimum volume
2. Maximum & minimum face angle
3. Edge length ratio
4. Element volume ratio
5. Connectivity ratio

It is also mentioned that it might not be possible for all meshes to satisfy all the criteria but they serve as general guidelines. Another important meshing parameter is y^+ which is represented by

$$y^+ = \frac{u_\tau \cdot y}{\nu}, \tag{3.1}$$

where y^+ is the non-dimensional wall distance, u_τ is the friction velocity at the wall, y is the distance from the first cell to the wall and ν is the kinematic viscosity [54]. This non-dimensional wall distance is used in CFD solvers to quantify the first cell height away from the wall and thus gives an indication of the mesh refinement near walls.

In CFD, the turbulent boundary layer close to a wall is often divided up into multiple regions or layers. These layers are the viscous sub-layer, buffer layer and log-law region. Figure 3.11 shows these regions with a profile for the non dimensional velocity U^+ as a function of the non dimensional wall distance y^+. This approximation is called the law of the wall and is used to model turbulent behavior close to the wall. In the outer layer, the flow is less influenced by the wall and the relation is not applicable. The black line on the figure represents the velocity profile as obtained from DNS simulation. The blue and green lines are empirical relations created to fit to this velocity profile. These are called wall functions and allow for approximation of the near wall turbulence instead of fully resolving thus greatly reducing the needed computational power. Depending on the distance from the wall as indicated by y^+, a different wall function should be used. The blue wall function fits well when $y^+ < 5$ while the green wall function fits well when using $y^+ > 30$.

Although these wall functions are handled and blended automatically by the CFD solver, it is important to note that the chosen y^+ should depend on the chosen turbulence model. Both the $k-\omega$ and $k-\omega$ SST model solve turbulence equations all the way to the wall or in the viscous sub-layer region. A $y^+ \approx 1$ is thus recommended with larger values resulting in the use of wall functions potentially reducing the accuracy in that region. The $k-\epsilon$ model for example relies on wall functions entirely resulting in a general recommended y^+ larger than 30 but smaller than 300 greatly reducing the needed mesh size [55].

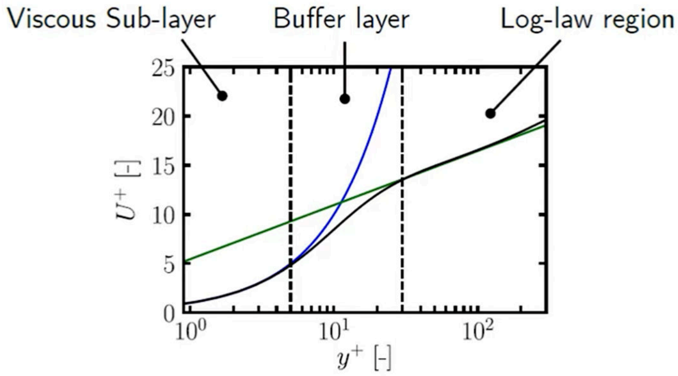

Figure 3.11: Law of the wall as visualized in [56].

Another meshing parameter that needs to be considered is the Reynolds number Re as shown in [57] where it is described by

$$Re = \frac{u \cdot L}{\nu} = \frac{\rho \cdot u \cdot L}{\mu}, \tag{3.2}$$

where ρ is the density of the fluid, u is the flow velocity, L is the characteristic length and μ is the dynamic viscosity of the fluid. Using air as a fluid and the operational conditions of the compressor, the Reynolds number can be estimated. When the Reynolds number increases, the friction velocity u_τ generally increases as well. This means the same y^+ will become smaller increasing the mesh size. A higher Reynolds for the same y^+ will thus result in a finer and more computationally demanding mesh. Using the SST turbulence model with the recommended y^+ of 1 will result in a greatly increased mesh size over a $k - \epsilon$ model with a larger y^+. A value for y^+ can be set in meshing software allowing the mesh to be adjusted accordingly. As this value is only an estimation, the actual range of y^+ on the simulated surfaces needs to be verified in Ansys CFD-Post after simulating a point.

A mesh independence study or grid convergence study will be done to ensure the mesh resolution is sufficient. The total-to-total pressure ratio π_{tt} and isentropic efficiency η_c will be simulated while increasing the mesh resolution until there are no significant changes in the result. To enable fair comparison between different operating and simulation conditions, the referred or corrected mass flow rate is used as described in [58] and given by equation:

$$\dot{m}_{corr} = \frac{W \cdot \sqrt{\theta}}{\delta}, \tag{3.3}$$

where $\dot{m}$ is the corrected mass flow rate in $\mathrm{kg/s}$, W is the mass flow rate in $\mathrm{kg/s}$, δ is the inlet pressure divided by the reference pressure and θ is the inlet temperature divided by the reference temperature. The reference conditions are $T_{ref} = 288.15\,\mathrm{K}$ and $p_{ref} = 101\,325\,\mathrm{Pa}$.

After the mesh quality is deemed sufficient, a convergence study is done similar to the mesh independence study. By increasing the residual target the pressure ratio and efficiency will be visualized until there are no large changes in the result.

3.4.5. Validation

To validate the CFD simulation, a pass-off result from an APS5000 APU validation test at EPCOR will be used. This test consists of a newly rebuilt APS5000 APU that is tested using various generator loads to validate the performance of the APU. Measurement points are taken at both nominal 100% speed and overspeed condition for different generator loads. A 100% speed point with nominal generator load is chosen as a reference point and will be used as a source of operating conditions as well as a validation reference for the CFD simulation. As each point is at a different generator load, only a single point is available at nominal operating conditions to validate the CFD simulation.

As the air mass flow rate of the test result is not measured in the test cell, an approximation is made using an energy balance and solving for one of the unknown mass flow rates. The gasses are considered ideal gasses and no bleed air is assumed. The energy balance is represented by

$$\dot{m}_2 \cdot h_2 + \dot{m}_f \cdot LHV = \dot{m}_5 \cdot h_5 + P_s, \tag{3.4}$$

where $\dot{m}_2$ and $\dot{m}_5$ are the mass flow rate at the compressor inlet and turbine outlet with $\dot{m}_f$ representing the fuel mass flow rate which is measured in the cell. The total enthalpy at the same locations is described by h_2 and h_5 with P_s being the shaft power. The lower heating value LHV of the Jet-A fuel is assumed to be $43\,031\,\mathrm{kJ/kg}$ as described in literature like [59]. The power taken from the shaft by the generators is estimated using

$$P_s = (S \cdot PF)/\eta_{gen}, \tag{3.5}$$

where P_s is the shaft power in kW, S is the apparent power in $\mathrm{kV\,A}$, PF is the power factor of the generators and η_{gen} is the generator efficiency. Using the nominal $450\,\mathrm{kV\,A}$ of the APU and assuming a PF of 0.9 with a $95\,\%$ generator efficiency results in a shaft power of $427\,\mathrm{kW}$ which is also used in the GSP model. The total enthalpy used in equation 3.4 at locations 2 and 5 is approximated using

$$h_{2,5} = C_{p_{2,5}} \cdot T_{t_{2,5}}, \tag{3.6}$$

where the average inlet temperature T_{t_2} is the average of 8 sensors at the APU inlet and the outlet temperature T_{t_5} is the average EGT measurement of 9 sensors at the turbine outlet. Specific heat capacity at the inlet C_{p_2} is assumed to be $1.006\,\mathrm{kJ/(kg\,K)}$. To estimate C_{p_5} of the exhaust gas, programs like NASA CEA can be used [60]. This value is however greatly dependent on the AFR or Air-Fuel Ratio. Assuming a stoichiometric air-fuel ratio results in a C_p of $1.2\,\mathrm{kJ/(kg\,K)}$ greatly reducing the estimated mass flow rate. As discussed in [61], modern gas turbines generally operate in lean conditions to reduce NO_x emissions. This results in excess air in the exhaust thus lowering the C_{p_5} and increasing the estimated mass flow rate. As the AFR is unknown the average C_p of air at the inlet and the exhaust gas at stoichiometric ratio at the outlet will be used resulting in a C_p of $1.1\,\mathrm{kJ/(kg\,K)}$. The isentropic compressor efficiency is estimated using the isentropic work divided by the actual work as described in

$$\eta_c = \frac{C_p \cdot T_{t_2} \cdot ((\frac{P_{t_2}}{P_{t_1}})^{(\frac{\gamma-1}{\gamma})} - 1)}{w_{actual}}, \tag{3.7}$$

where C_p is the average of the compressor inlet and outlet C_p given the temperature and pressure resulting in $1.044\,\mathrm{kJ/(kg\,K)}$. The specific heat ratio γ is assumed to be 1.4 and the actual work w_{actual} is calculated using the enthalpy difference as given in

$$w_{actual} = h_3 - h_2, \tag{3.8}$$

where the total enthalpy h_3 is calculated using equation 3.6 with the compressor outlet temperature T_{t_3} as measured in the test cell.

3.4.6. Reverse Engineering

To simulate the performance of a new and used compressor stage, the geometries need to be imported in the chosen CFD software. As the geometry of the impeller and diffuser are not available, they need to be 3D scanned and converted to the appropriate file type. Having the geometry in a CAD or computer-Aided Design format would allow it to be used with most CFD tools. Ansys TurboGrid on the other hand, only supports either .curve files from Ansys BladeGen or a CAD file import using Ansys DesignModeler where the geometry is redrawn into an Ansys specific file type. EPCOR has an ATOS scanning booth as shown in Figure 3.12 where parts like the shown impeller in Figure 3.13, can be scanned. This 3D scan generates a triangulated mesh in the form of a .STL file. Although there are software tools like Geomagic that try to convert a 3D scan to a CAD file automatically, they still need some user input. An example of this is shown in [62] where the workflow mostly consists of reconstructing the needed part by using references and curves from the 3D scan. A SolidWorks plug-in called QuickSurface is found to allow approximation of complicated curves like the impeller blades while the rest of the geometry can be reconstructed manually using measurements from the 3D scan. The reverse engineering workflow is thus heavily dependant on both the chosen mesher and CFD software. The final workflow would preferably also include an overlay where the constructed CAD file is overlaid with the 3D scan to see how much the reconstructed geometry deviates.

Figure 3.12: EPCOR ATOS scanbox.

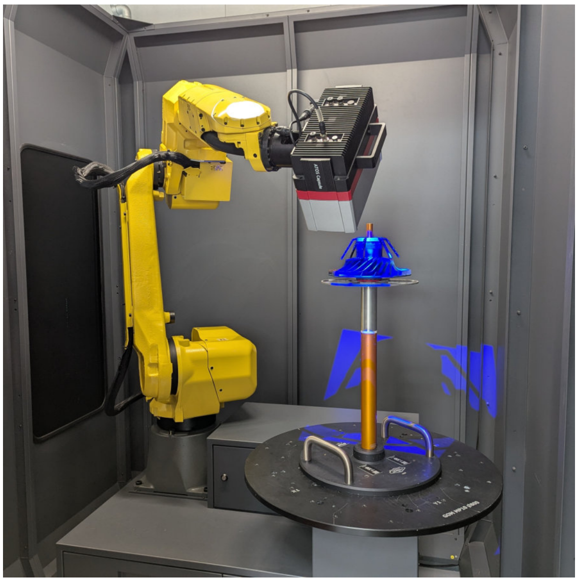

Figure 3.13: Impeller scanning setup.

3.4.7. Modeling of compressor deterioration effects

Tip Clearance

Tip clearance can be simulated by leaving a gap between the impeller shroud and diffuser. In Ansys Turbogrid for example, the shroud tip clearance can be set directly. This distance can be set as the normal distance resulting in an equal tip clearance along the full span of the blade or it can be set using a variable tip clearance where the leading edge and trailing edge distance is set separately. More options are available but they do not give fine control over the tip clearance distance.

Surface Roughness

To quantify the surface roughness in fluid dynamics or CFD solvers, a sand grain roughness parameter or k_s is used. This parameter is dependent on a number of statistical variables like the roughness height, roughness skewness and roughness kurtosis which describes the height distribution [31]. As seen in most sources discussing surface roughness, the empirical relation to quantify k_s is often related using a measured surface roughness like the average surface roughness R_a or the Root Mean Square value R_{rms} which can both be measured using a profilometer. Sources like [36] discuss the performance deterioration as a result of surface roughness and use empirical relations to estimate the k_s from the surface roughness R_a with this source using the relation $k_s = 6.2 \cdot R_a$ originating from [63]. The sand grain roughness can also be estimated using an algorithm as shown in [64], resulting in the relation $k_s = 5.863 \cdot R_a$.

Both sources [6] and [31] include substantial tables with empirical relations to estimate k_s in gas turbines from both experimental as well as CFD simulated research. In the conclusion of the former source it is said that the use of the k_s parameter hampers modeling as it does not account for different roughness effects on skin friction, boundary layer transition and heat transfer. The latter source concludes that the sand grain roughness fails to completely characterize roughness in many cases as it is dependent on many variables. Moreover, source [65] as reported in [6] concludes that the most used estimations of k_s vary up to an order of magnitude depending on the chosen empirical relation. As there is no single consensus on the empirical relation to estimate k_s, the relation $k_s = 5.863 \cdot R_a$ from [64] will be used. It aligns with the previously mentioned relation $k_s = 6.2 \cdot R_a$ from [36] where compressor performance deterioration as a result of erosion is modeled and validated with test data.

Modeling and simulating particle ingress to estimate erosion locations and surfaces with increased roughness is studied in literature with reference [66] trying to simulate and predict erosive wear locations while source [67] simulates particle trajectories in a centrifugal compressor. To simplify the problem, the simulated surfaces with increased surface roughness will be chosen as visually seen from a worn impeller.

To simulate the effect of surface roughness on the APU compressor stage the average surface roughness or R_a will be measured with a profilometer for both a new and worn impeller. By using the relation $k_s = 5.863 \cdot R_a$, the sand grain roughness is quantified and used in the chosen CFD solver on the compressor surfaces where fouling and increased surface roughness is seen. The performance impact on the APU as a result of increased surface roughness can then be simulated.

4

Compressor model development

4.1. Geometry modeling

In this section, the reverse engineering process used to model both the impeller and vaned diffuser of the compressor stage is discussed.

4.1.1. Impeller scanning

Using the ATOS scanbox, a high fidelity scan of an unused impeller is taken and exported as a .STL file. The original scan contains a triangulated impeller mesh consisting of 47.5 million polygons and a file size of $2.32\,\mathrm{GB}$, making it very slow to work with. A reduced version was exported by EPCOR consisting of a $171.5\,\mathrm{MB}$ file size and 3.5 million polygons. Figure 4.1 shows the original 3D scan with Figure 4.2 showing a rendered version of the impeller. As the impeller needs to be scanned from different angles and sides it is spun around in the scanning booth by setting it on a custom piece resulting in the bottom of the geometry not being scanned perfectly. This results in open edges increasing the number of polygons while not contributing to the geometry. Figure 4.4 shows the bottom of the impeller and some floating surfaces with open edges being indicate in purple. Figure 4.5 shows a hole in the scan on one of the impeller blades. These open edges result in a high number of polygons that do not increase the detail of the geometry.

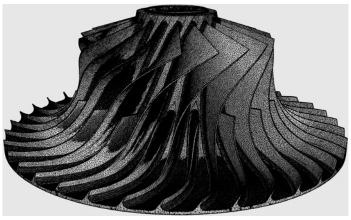

Figure 4.1: High fidelity impeller 3D scan.

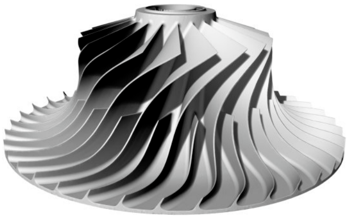

Figure 4.2: Render of high fidelity impeller 3D scan.

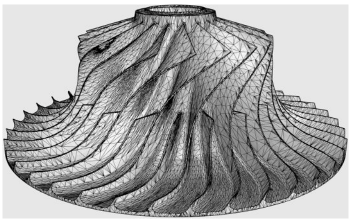

Figure 4.3: Reduced and cleaned impeller 3D scan.

The mesh is cleaned up manually using Rhinoceros 3D or Rhino. After deleting floating polygons and most of the bottom side of the impeller, the mesh is closed by manually inserting mesh faces. A closed mesh is needed as most CAD software like Solidworks will convert a .STL file to a surface or body. Because of each polygon being saved as a surface, importing the geometry into CAD software causes a long load time. The same happens when saving the .STL as a .STEP file which also increases the file size. This introduced the need to further reduce the file size. Using the *ReduceMesh* command in Rhino the mesh is reduced to 90757 polygons with a file size of $4.4\,\mathrm{MB}$ which is shown in Figure 4.3. The scan is now closed, has no errors, and can be imported into the preferred CAD tool.

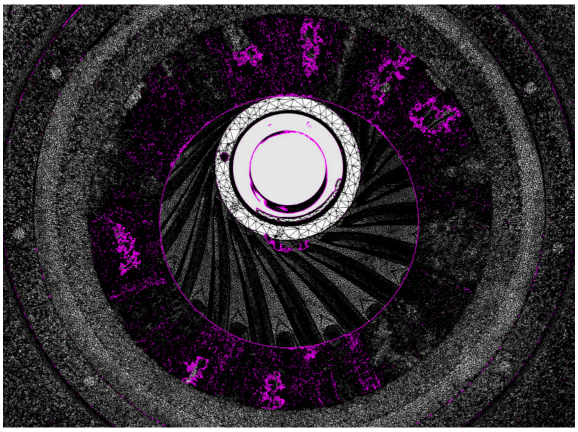

Figure 4.4: Bottom surface with open edges.

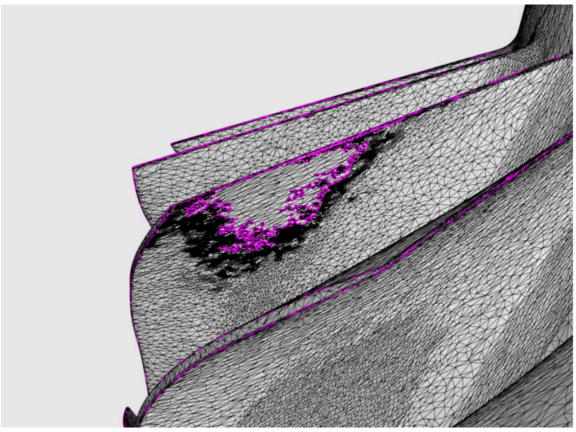

Figure 4.5: Impeller blade hole with open edges.

4.1.2. 3D Modeling

As a scan or mesh cannot directly be used in Ansys CFX, an Ansys BladeGen model needs to be made. To measure the required impeller geometry parameters, a 3D model of the impeller is made in SolidWorks. The reduced mesh is converted to a surface using the *MeshToNurbs* Rhino command allowing for a faster import in SolidWorks. Section views for both the hub, main blade and splitter blade outlines from the 3D scan are used as a reference to model the impeller. The shape of the blades is approximated by a surfacing tool called QuickSurface. The final 3D model is not a perfect representation of the original geometry but is used to measure the needed parameters of the impeller.

4.1.3. Ansys BladeGen

Impeller

Using the 3D model, the dimensions of the impeller can be measured to recreate it in Ansys BladeGen. Ansys Workbench is used to connect Ansys BladeGen with Ansys Turbogrid allowing the recreated geometry to be imported and updated easily. Using the measured dimensions a rough start of the impeller model is made. Feeding both the Ansys BladeGen model and the original 3D scan into Ansys DesignModeler allows for comparison by overlaying the geometries as shown in Figure 4.6 where the BladeGen model is shown using different blade colors and the 3D scan is shown by the orange mesh. As the BladeGen model in DesignModeler automatically updates when it is changed, the model parameters can be changed until a good visual match between the BladeGen model and the 3D scan is made. Making a 3D model in CAD is thus not necessary and is omitted when making a BladeGen model for the diffuser.

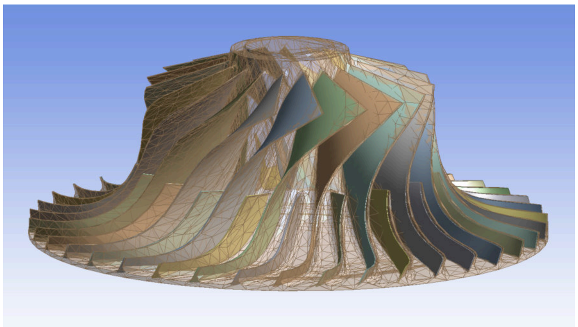

Figure 4.6: Impeller 3D scan overlaid with BladeGen model.

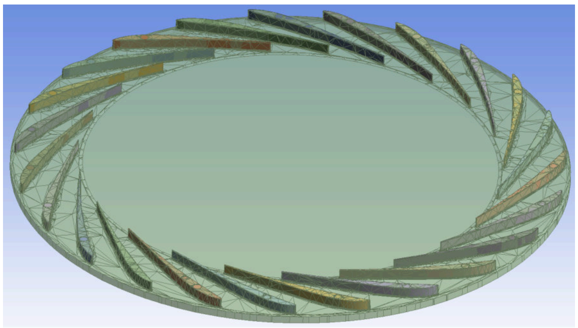

Figure 4.7: Diffuser 3D overlaid with BladeGen model.

Vaned Diffuser

After initial simulations only containing the impeller, the vaned diffuser is added to the simulation domain. The 3D scan of the compressor diffuser is shown in Figure 4.8. To simplify the BladeGen model, only the diffuser vane in the same plane as the impeller is added to the domain with the guide vane after the diffuser bend being cut off as shown in Figure 4.9. Similar to what was done with the impeller, Figure 4.9 shows the reduced and cleaned up scan converted to a surface model using Rhino. From reverse engineering the impeller, it was clear that the simplest way of constructing the BladeGen model is to start from rough dimension taken straight from the 3D scan after which the scan can be overlaid with the BladeGen model to visually adjust the BladeGen dimensions as shown in Figure 4.7. The diffuser is not reverse engineered in Solidworks as it does not provide a benefit over what is available from the scan.

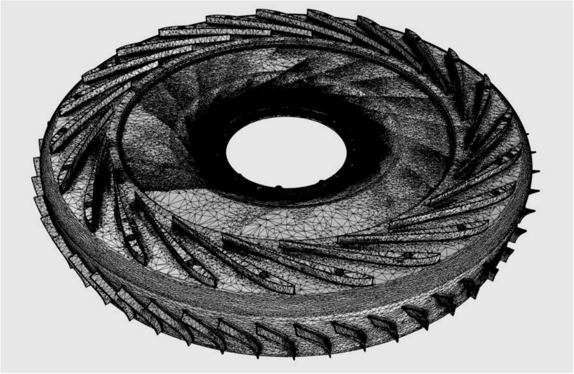

Figure 4.8: Diffuser 3D scan.

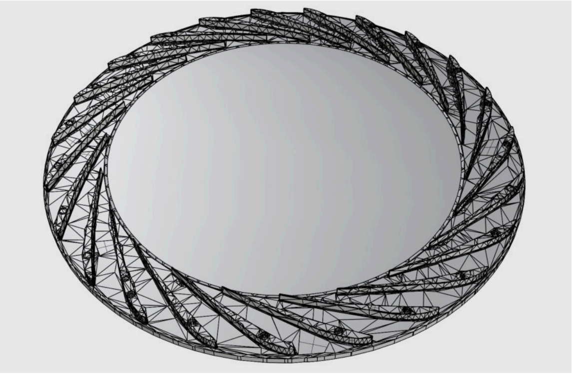

Figure 4.9: Reduced and cut diffuser 3D scan.

4.2. CFD modeling

In this section the constructed CFD model is discussed.

4.2.1. Simulation Setup

Due to the simple integration between the different Ansys software packages, Ansys CFX is chosen as the CFD software with Turbogrid being used as the meshing software. Ansys Workbench is used to connect the various software packages where the constructed BladeGen model is fed into Turbogrid, after which the mesh is fed into CFX-pre to set up and run the simulation.

A steady state simulation assuming air as an ideal gas is performed on a single vane passage. Periodicity is used for both the impeller and diffuser with a mixing plane interface in between. The simulated domain is shown in Figure 4.11. Using the pass off test result as a reference point, the total inlet temperature is set to $278.8\,\mathrm{K}$, the rotational speed is set to $35\,409$ rpm with the total-to-total pressure ratio used in 4.2.4 to validate the simulation. In terms of boundary conditions, the mass flow rate at the inlet is varied while the static pressure at the outlet is set to $7.6\,\mathrm{bar}$ to match the outlet pressure of the reference point. A constant span nominal shroud tip clearance is set as $1.7\,\mathrm{mm}$ as this is the middle value of the cold tip clearance during compressor assembly. During initial simulations, the surfaces were set to smooth meaning no surface roughness. The turbulence intensity at the inlet is set to the medium value of $5\,\%$ as generally recommended and shown by a similar case in [68]. In terms of the CFX solver settings, most options are left as standard. This means a high resolution advection scheme and first order turbulence numerics are used. However, the double precision solver option is enabled.

To construct a speed line and evaluate the performance of the compressor stage at various mass flow rates, the inlet mass flow rate is varied in 10 steps. Initially, only the impeller was simulated to reduce the computational power needed and to verify if the modeled geometry can achieve performance similar to the test result. Using the SST turbulence model the impeller showed a significantly lower pressure ratio compared to the test points. Switching to the $k-\epsilon$ turbulence model closely aligned the simulated pressure ratio with the test result. Sources like [24], [37] and [66], indicate that the $k-\epsilon$ model is often adequately accurate to evaluate turbomachinery performance.

After adding the diffuser, another simulation using the SST turbulence model using a finer mesh was tested. Due to the high Reynolds number, the recommended y^+ of 1 resulted in a mesh that was too big for the available computational power. The $k-\epsilon$ model is deemed more appropriate for the application and is used for the remaining simulations.

4.2.2. Meshing & Grid independence Study

Ansys TurboGrid is used to mesh both the impeller and diffuser resulting in a structured hexahedral mesh for both components. The standard Turbogrid mesh limits are used to evaluate the mesh quality.

To ensure the meshed is of adequate resolution, a grid or mesh independence study is carried out. The same 10 mass flow points will be simulated after which the pressure ratio and isentropic compressor efficiency are visualized. The global size factor of the mesh is then increased until the simulated results no longer change significantly indicating that the solution is gid independent. When increasing the global size factor of the impeller mesh the diffuser mesh global size factor is increased the same amount to make sure there are no large cell discrepancies between the meshes. Table 4.1 shows the global size factor as well as the resulting mesh sizes for 5 different meshes with Figure 4.10 showing the resulting simulated points.

As mentioned in 3.4.4, TurboGrid allows setting an offset y^+ value after which it estimates the near wall spacing in the boundary layer using a formula largely depending on the Reynolds number. As this Reynolds number is an approximation, the actual y^+ as calculated by the solver can vary from the estimated offset. After simulating a point, a y^+ contour plot for both the impeller and diffuser is generated in CFD-Post to verify the actual y^+ of the mesh. Not only the simulated speed lines but also the actual y^+ is taken into account to choose the correct mesh resolution.

As shown in Figure 4.10, step 4 and 5 show very similar values until the compressor approaches surge conditions. The y^+ contour of step 4 is shown in Figure 4.12 where it can be seen that the actual y^+ of the domain is within the recommended 30 and 300 for the $k-\epsilon$ model. As CFX uses scalable wall functions with the $k-\epsilon$ model as standard, this large y^+ variation is accounted for. This mesh is thus used moving forward.

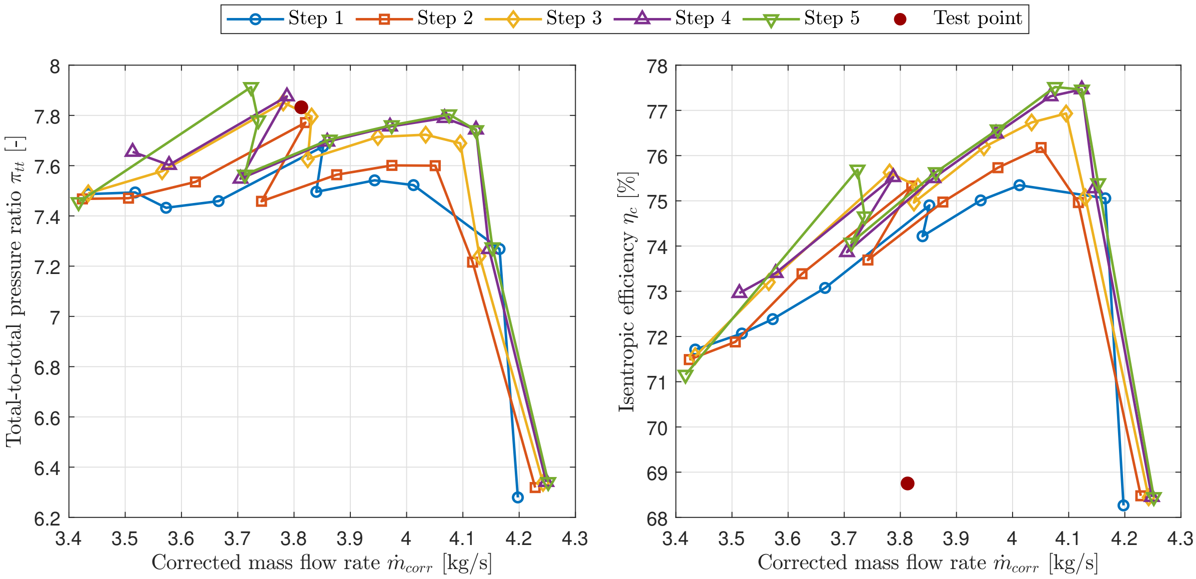

Figure 4.10: Total-to-total pressure ratio and isentropic compressor efficiency as a function of mass flow rate for increasing mesh sizes.

	Global size factor	Impeller nodes	Diffuser nodes	Total mesh size
Step 1	1	346366	68300	414666
Step 2	1.3	662080	145652	807732
Step 3	1.6	1187754	247349	1435103
Step 4	1.9	1764120	384984	2149104
Step 5	2.15	2328880	536640	2865520

Table 4.1: Mesh resolution steps.

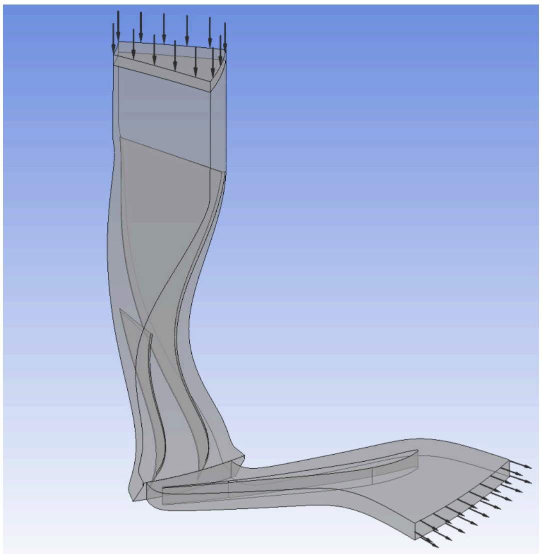

Figure 4.11: Simulated compressor domain in CFX.

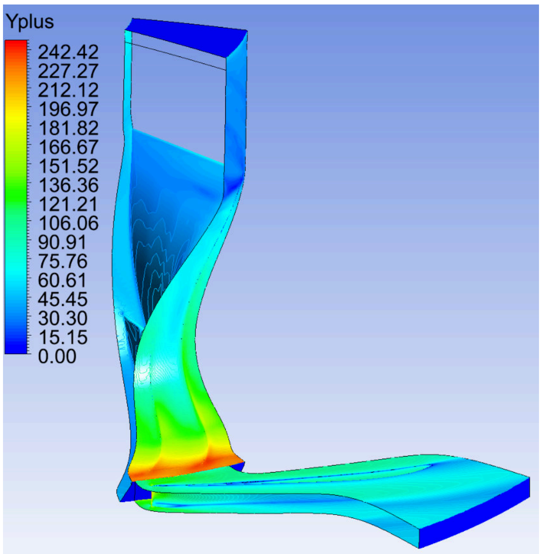

Figure 4.12: Actual y^+ for the step 4 mesh.

4.2.3. Convergence tolerance analysis

After the mesh was deemed sufficiently fine, the convergence residuals of the solver are increased to make sure the solution is adequately solved. Figure 4.13 shows the previously chosen step 4 mesh for increasing solver residuals. Both Figures 4.10 and 4.13 show that the previously used Root Mean Square or RMS of $5e^{-5}$ was not adequately solved as the pressure ratio and efficiency show large fluctuations when approaching surge. When increasing the residuals, the fluctuations reduce while the lowest mass flow point containing a converged solution increases as the compressor approaches surge. The finest residuals of $5e^{-6}$ were chosen and used for the CFD simulations.

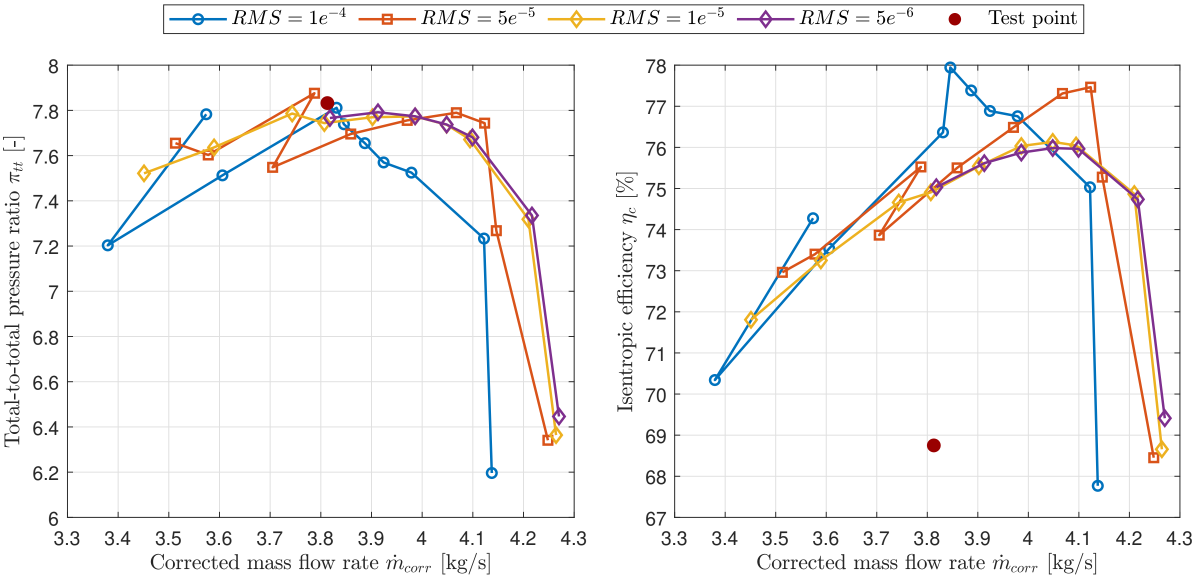

Figure 4.13: Total-to-total pressure ratio and isentropic compressor efficiency as a function of mass flow rate for increasing solver residuals.

4.2.4. Validation

To validate the CFD model, a comparison between the simulation and test result pressure ratio and efficiency is made in Figure 4.14. The simulated pressure ratio at the lowest mass flow point of the compressor stage without deterioration effects is 7.77 aligning well with the 7.83 pressure ratio of the test result. In terms of mass flow rate, the test result shows $3.81\,\mathrm{kg/s}$ with the lowest mass flow rate of the simulation being $3.82\,\mathrm{kg/s}$. Although the calculated test result mass flow rate is close to the surge condition of the CFD simulation, applying a surface roughness to the simulation reduces the flow capacity. This shifts the speed line towards the left bringing the test result closer to a realistic operating region. The mass flow rate calculation of the test cell data carries some uncertainty due to the assumed exhaust gas heat capacity C_{p_5}. The assumed $C_{p_5} = 1.1$ results in a corrected mass flow rate of $3.81\,\mathrm{kg/s}$ whereas a leaner exhaust gas with a $C_{p_5} = 1.05$ would result in a significantly higher corrected mass flow rate of $4.10\,\mathrm{kg/s}$. Another uncertainty is the inaccuracy of the test cell fuel flow sensors which was mentioned by the EPCOR technicians.

In terms of the isentropic efficiency a larger difference between the simulation and test result is seen. At the lowest mass flow rate the simulation overestimates the test result by $6.28\,\%$ and up to $7.23\,\%$ at higher mass flow rates. This can be attributed to the $k - \epsilon$ turbulence model as it is known to struggle with adverse pressure gradients, underestimating flow separation resulting in an overestimated efficiency. As the objective of this study is to evaluate the relative performance differences resulting from compressor deterioration, the absolute deviation from the experimental data is of less importance. Therefore, the CFD model is considered suitable for performing a sensitivity analysis despite the limited availability of test data.

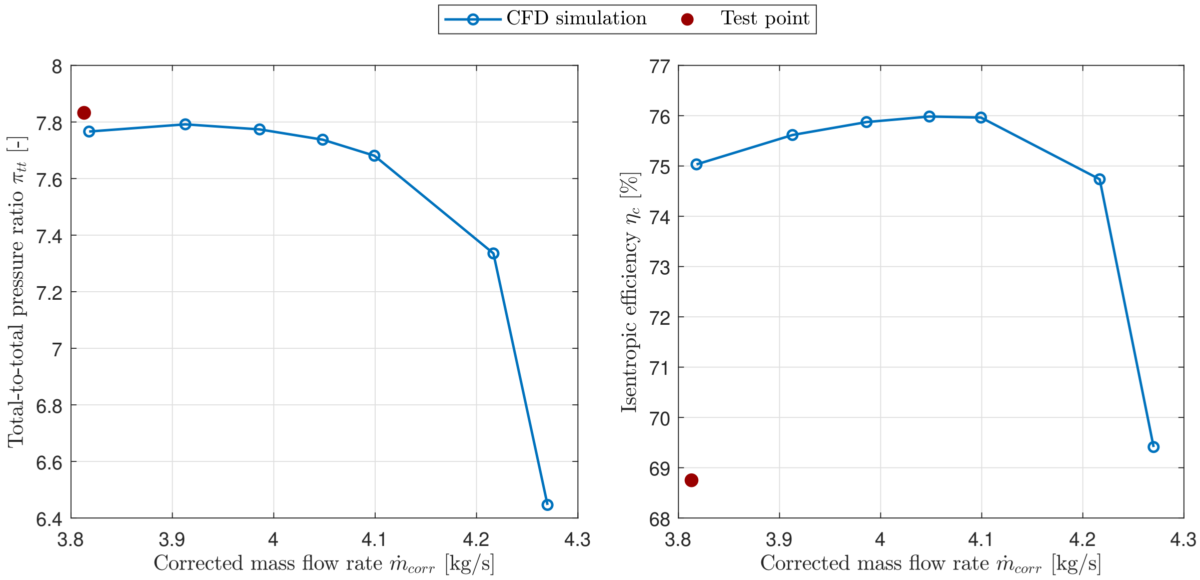

Figure 4.14: Simulated Total-to-total pressure ratio and isentropic compressor efficiency as a function of mass flow rate compared to test result.

4.2.5. Deterioration effects modeling

With the validated model including sufficient mesh resolution and convergence criteria, the deterioration effects can now be added. To evaluate the performance impact of tip clearance and surface roughness, the same speed line consisting of 10 different mass flow points will be simulated using different tip clearances, geometry surface roughness or both. To simulate the deterioration effects, 2 impellers will be used as reference. A used but cleaned impeller that is within the desired specification to be used again will be considered the clean impeller. This clean impeller is shown in Figure 4.15. Figure 4.16 shows a used and damaged impeller with a deformed blade and leading edge chipping as previously shown in Figures 3.4 and 3.5. Although the geometry of this impeller is heavily damaged, it only ran half the amount of hours APU's normally run before overhaul, which likely results in reduced fouling and surface roughness. This impeller will be considered as the used or dirty impeller.

Figure 4.15: Within specification cleaned impeller.

Figure 4.16: Used and unwashed impeller.

Surface roughness

To simulate the performance impact of the surface roughness on the compressor stage, the surface roughness of the impeller is measured using a PCE-RT 1200 profilometer as shown in Figure 4.17. By dragging a fine diamond tip over a surface the profilometer measures the surface profile. It is calibrated with a calibration plate by measuring the surface roughness of the plate and adjusting the gain to match the result to the value on the calibration plate. The profilometer is set to evaluate the average surface roughness R_a using a sampling length of $0.8\,\mathrm{mm}$ with an evaluation length of 5. This results in a measurement being the average value of 5 samples each spanning $0.8\,\mathrm{mm}$ totaling a length of $4\,\mathrm{mm}$. As there is no test setup available and the profilometer can only measure a straight surface, the suction side of the impeller $\pm 4\,\mathrm{mm}$ from the leading edge is measured as shown in Figure 4.18.

Figure 4.17: PCE-RT 1200 profilometer and calibration plate..

Figure 4.18: Surface roughness measurement close to leading edge of impeller..

The same area on the impeller is measured 3 times after which the average R_a value is taken to calculate the sand grain roughness k_s. For the used impeller an extra measurement as close as possible to the leading is taken as there is visibly increased surface roughness as previously shown on Figure 3.4. The results of the surface roughness measurements are shown in Table 4.2 with the used impeller showing a $50.1\,\%$ increase in surface roughness at the same location. The extra measurement close to the leading of the impeller shows another $17.5\,\%$ increase in average surface roughness.

Measurement	Meas. 1 $[\mu m]$	Meas. 2 $[\mu m]$	Meas. 3 $[\mu m]$	Avg. R_a $[\mu m]$	k_s $[\mu m]$
Clean	0.629	0.641	0.647	0.639	3.688
Used	1.021	0.944	0.913	0.959	5.623
Used (leading edge)	1.195	1.128	1.058	1.127	6.608

Table 4.2: Measured surface roughness for both the clean and used impeller.

This calculated sand grain parameter k_s is directly used in Ansys CFX to simulate surface roughness. The roughness is applied to both impeller and diffuser together as well as separately to evaluate the performance sensitivity of both components individually as well as the overall compressor. All surface roughness simulations are performed using the nominal tip clearance of $1.7\,\mathrm{mm}$. Initial simulations using the clean sand grain roughness of $3.688\,\mu\mathrm{m}$ on all impeller and diffuser surfaces showed a large reduction in pressure ratio and isentropic efficiency as shown in Figure 5.1. Setting the shroud as a smooth surface reduced this pressure and efficiency loss by more than half. The compressor shroud is made of a different material than the impeller and diffuser and generally does not suffer from increasing surface roughness. Local increased surface roughness as a result of impeller rubbing can occur but this is considered insignificant. As the simulated performance impact is very large, the shroud for both the impeller and diffuser is considered smooth to eliminate this effect from the simulation. Including simulations for a further increased roughness using $k_s = 10\,\mu\mathrm{m}$ and adding it to the tip clearance simulations results in a test matrix as shown in Table 4.2.

Case ID	k_s $[\mu m]$	Impeller surfaces	Diffuser surfaces	Tip clearance $[mm]$
1	3.688	Blade, hub	Blade, hub	1.7
1	5.623	Blade, hub	Blade, hub	1.7
1	10	Blade, hub	Blade, hub	1.7
2	3.688	Blade, hub	-	1.7
2	5.623	Blade, hub	-	1.7
2	10	Blade, hub	-	1.7
3	3.688	-	Blade, hub	1.7
3	5.623	-	Blade, hub	1.7
3	10	-	Blade, hub	1.7
4	3.688	Blade, hub	Blade, hub	1.4
4	3.688	Blade, hub	Blade, hub	1.7
4	3.688	Blade, hub	Blade, hub	2.0
4	3.688	Blade, hub	Blade, hub	2.3
5	3.688	Blade, hub	Blade, hub	2.0
5	5.623	Blade, hub	Blade, hub	2.0
5	10	Blade, hub	Blade, hub	2.0
6	3.688	Blade, hub	Blade, hub	2.3
6	5.623	Blade, hub	Blade, hub	2.3
6	10	Blade, hub	Blade, hub	2.3

Table 4.3: Simulation test matrix.

Tip clearance

As the running tip clearance is difficult to determine, a range of tip clearances using $0.3\,\mathrm{mm}$ steps increasing and decreasing from the nominal $1.7\,\mathrm{mm}$ cold clearance will be simulated. The tip clearance is assumed to be constant span. A test matrix containing the various simulations is shown in Table 4.3. In terms of surface roughness, the sand grain roughness of the clean impeller is used on both the impeller and diffuser blades and hub.

4.3. System performance

To evaluate the APU system performance degradation as a result of compressor deterioration, a GSP model is used to simulate a gas turbine and evaluate the relative difference in fuel flow, pressure ratio and EGT. GSP is a component modeling tool that can be used to model various configurations of gas turbine engines. The program models the thermodynamic cycle of a gas turbine using 0D modeling, which means the flow properties are averaged over flow cross section areas between the interfaces of the components. A design point with certain parameters is used as a reference point, after which an off design analysis using a deteriorated compressor can be performed to evaluate the performance difference. To calculate the performance of this design point, a compressor map is needed. The turbine uses a generic map that is available in GSP.

4.3.1. Compressor map generation

As there is no compressor map available, a map is made using a single speed line from the smooth impeller and diffuser CFD simulation as shown by the blue line in Figure 5.1. GSP needs a full map so a 0.9 and 1.1 corrected speed line is made by multiplying the pressure ratio and mass flow rate by a scaling factor. The GSP simulation is performed at International Standard Atmosphere or ISA conditions and constant rotational speed to ensure the compressor operates on the $N_c = 1$ speed line making the other speed lines irrelevant. When introducing compressor deterioration, GSP scales the compressor map as the compressor behavior changes. The final compressor map is shown in Figure 4.19.

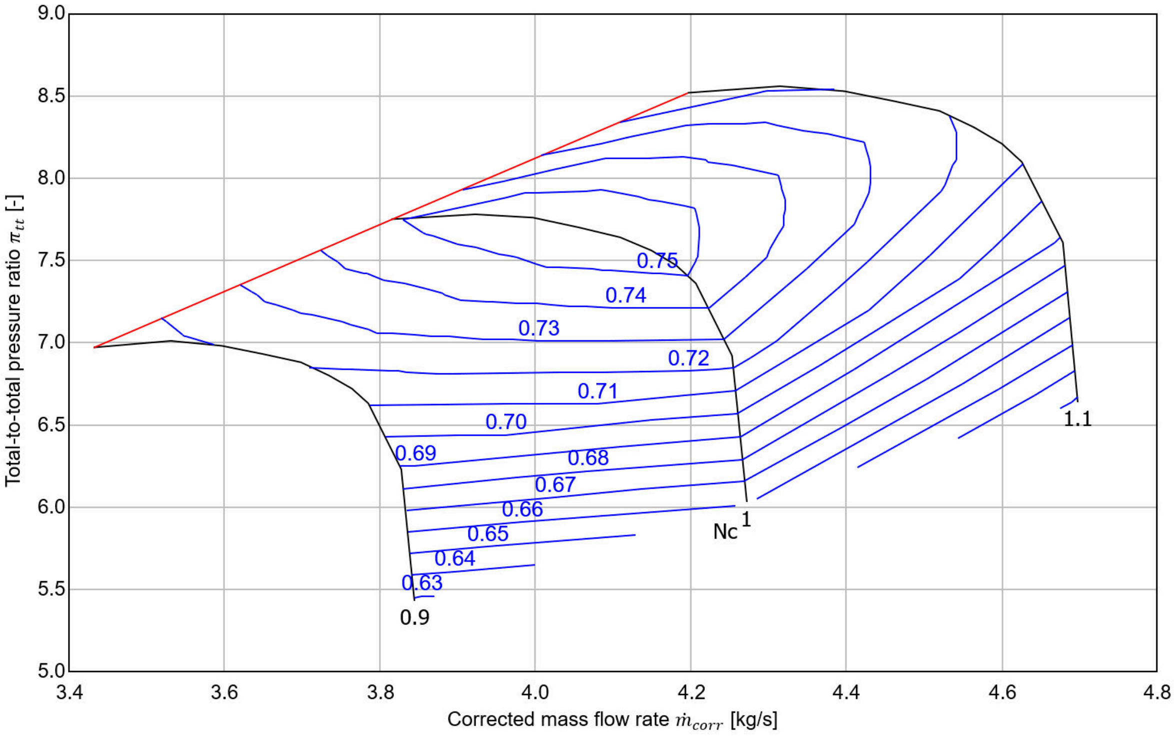

Figure 4.19: GSP compressor map made using smooth CFD result.

4.3.2. GSP performance deterioration

In GSP, compressor deterioration is defined in the deterioration tab, where reductions in flow capacity $d\dot{m}corr$ and isentropic compressor efficiency $d\eta_c$ relative to the design point are specified. These reductions are derived from the CFD simulated performance lines where the flow capacity $d\dot{m}_{corr}$ is estimated using the average reduction in mass flow rate between the smooth and deteriorated lines while the reduction in efficiency $d\eta_c$ is the difference between the smooth and deteriorated lines at the mass flow rate of the design point. After simulating the design point, the efficiency and flow capacity deterioration are used in an off design simulation to calculate the relative performance difference in fuel flow dW_f, exhaust gas temperature $dEGT$ and pressure ratio $d\pi_{tt}$. To take into account the ambient pressure, the relative percentage difference in pressure ratio is calculated using

$$d\pi_{tt} = \frac{\pi_{tt2} - \pi_{tt1}}{\pi_{tt1} - 1} \cdot 100, \tag{4.1}$$

where $d\pi_{tt}$ is the relative percentage difference in pressure ratio, π_{tt2} is the new pressure ratio and π_{tt1} is the reference pressure ratio.

The design point parameters of the GSP model are taken from different simulated results depending on the surface roughness or tip clearance comparison. The relative performance difference with increasing surface roughness is evaluated against the simulated result with nominal tip clearance and smooth geometries, with the corresponding design point or DP parameters provided in column 2 of Table 4.4. The relative performance difference with increasing tip clearance is compared to the base roughness of $3.688\,\mu\mathrm{m}$ at nominal tip clearance $1.7\,\mathrm{mm}$ which is shown in column 3 of Table 4.4. As mentioned in 3.4.5, turbine external load is calculated and set using the $427\,\mathrm{kW}$ from the test point. The rotor speed n is kept constant and corrected to ISA conditions based on the test result, corresponding to a rotor speed of $36\,000\,\mathrm{rpm}$, which equals a corrected speed of $N_c = 1$.

Variable	Surface roughness DP	Tip clearance DP
Total-to-Total pressure ratio π_{tt} [-]	7.78	7.66
Corrected mass flow rate $\dot{m}_{corr}$ $[\mathrm{kg/s}]$	3.94	3.94
Isentropic efficiency η_c $[\%]$	75.66	74.84
Shaft power P_{shaft} $[\mathrm{kW}]$	427.00	427.00
Rotor speed n $[\mathrm{rpm}]$	36000.00	36000.00

Table 4.4: Gas turbine simulation design point parameters.

5

Results

5.1. Compressor performance

In this section, the simulated results of the compressor are shown. The performance and flow capacity loss is evaluated using the average relative difference between the different curves. The difference only includes operating conditions that are present in both curves. In terms of pressure ratio and efficiency the difference in y-axis for the same mass flow conditions is considered with the flow capacity using the difference in x-axis on the pressure ratio plot.

5.1.1. Surface roughness effects

Shroud surface roughness

As previously mentioned in 4.2.5, including the shroud to the surfaces with increased surface roughness greatly increases the pressure ratio and efficiency loss compared to a smooth shroud. Figure 5.1 shows the pressure ratio and compressor efficiency using the clean impeller surface roughness value for both the impeller and diffuser geometries with and without shroud roughness. Including the shroud surface roughness results in an average pressure ratio reduction of 0.44 or $5.71\,\%$ and an average loss of $2.81\,\%$ in isentropic efficiency compared to the smooth geometry.

Removing the surface roughness of the shroud from both impeller and diffuser results in a 0.19 or $2.50\,\%$ loss in pressure ratio with a $1.29\,\%$ loss in efficiency compared to the smooth geometries. The remaining simulations as indicated in Table 4.3 all consist of a smooth shroud.

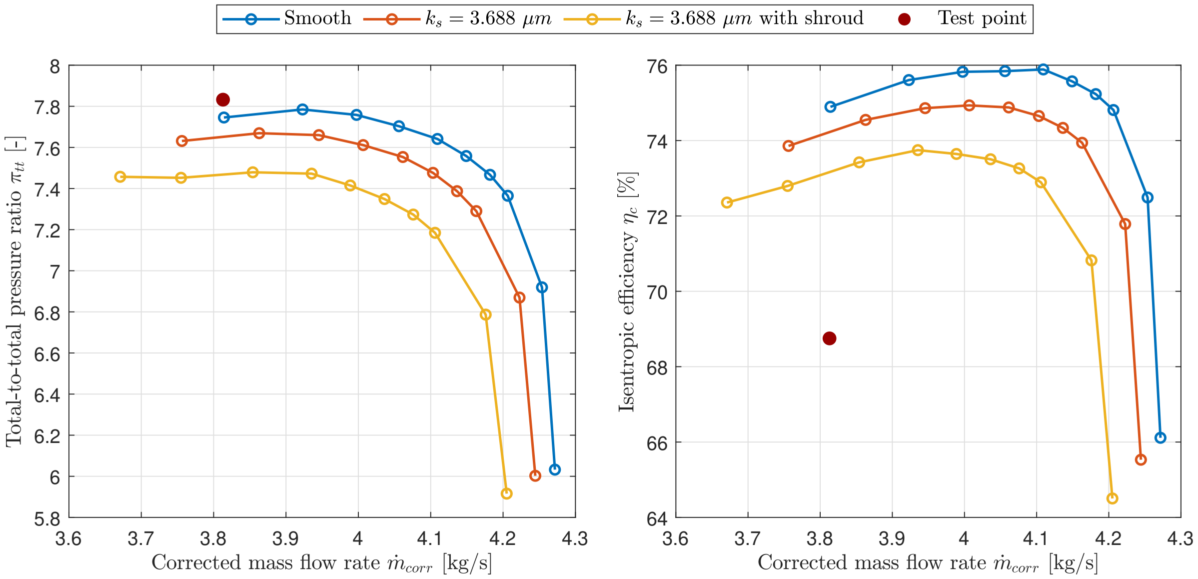

Figure 5.1: Simulated total-to-total pressure ratio and isentropic compressor efficiency as a function of mass flow rate comparing a smooth shroud and a shroud with surface roughness.

Case ID 1: Compressor roughness

Using a smooth shroud and 3 different levels of surface roughness for the impeller and diffuser hub and blades results in Figure 5.2. Increasing surface roughness results in a reduction in pressure ratio, efficiency and flow capacity as expected with the overall shape of the speed lines staying consistent. The lowest mass flow rate condition of the $5.623\,\mu\mathrm{m}$ speed line shows an inconsistent result as it overlaps with the $3.688\,\mu\mathrm{m}$ point. Table 5.1 summarizes both the relative losses in pressure ratio, efficiency and flow capacity compared to the smooth curve as well as the relative loss per $\mu\mathrm{m}$ of surface roughness. Figure 5.6 plots this trend to visualize the sensitivity of these parameters which indicates that the losses of the impeller and diffuser simulations scale almost linearly with surface roughness, although the rate of loss in pressure ratio and efficiency reduces at higher roughness values.

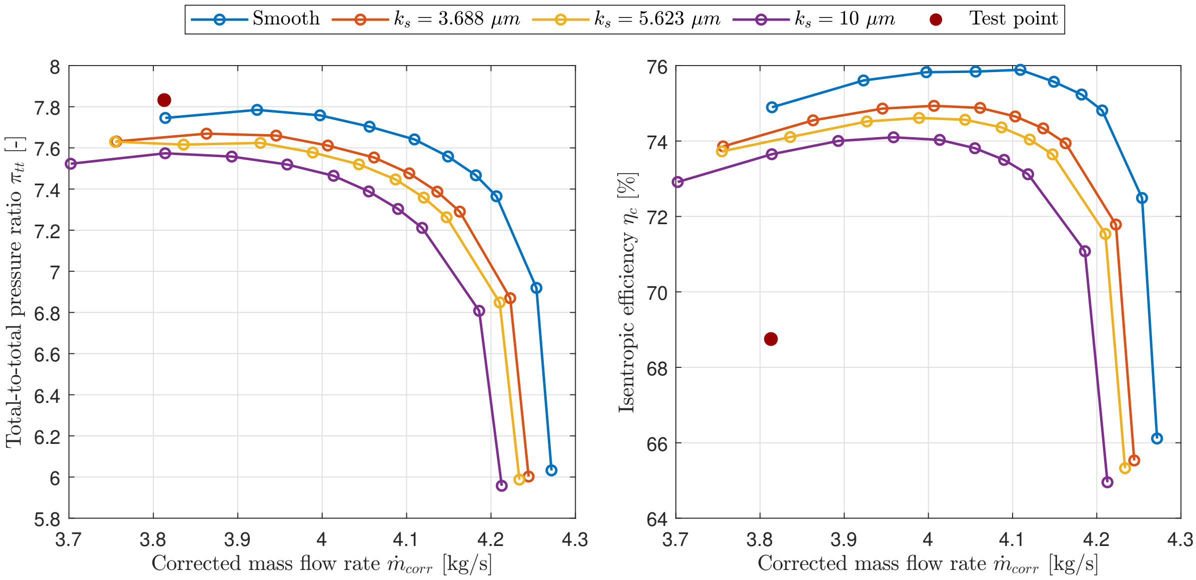

Figure 5.2: Simulated total-to-total pressure ratio and isentropic compressor efficiency as a function of mass flow rate for increasing surface roughness on impeller and diffuser blades and hub.

Case ID 2: Impeller roughness

Doing the same for only the impeller surface roughness results in Figure 5.3 showing a similar result with less pressure ratio, efficiency and flow capacity losses. The surface roughness sensitivity shown in Figure 5.6 indicates that the impeller loses less efficiency and pressure ratio but more flow capacity compared to only the diffuser simulation. Similar to the impeller and diffuser simulation, the relation of losses with surface roughness is almost linear but the rate of loss reduces at higher surface roughness.

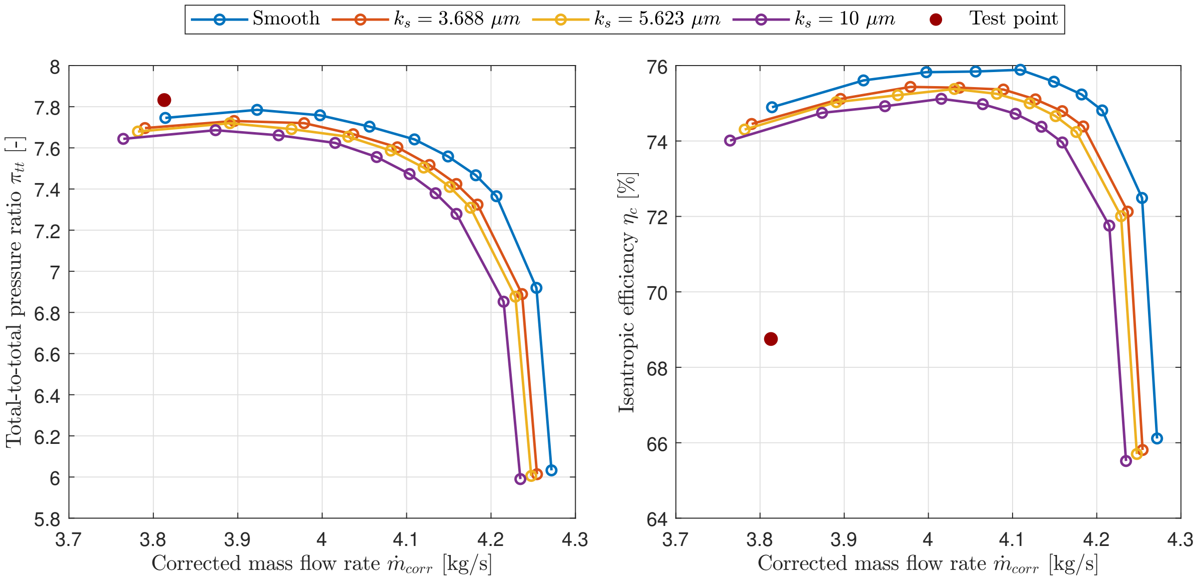

Figure 5.3: Simulated total-to-total pressure ratio and isentropic compressor efficiency as a function of mass flow rate for increasing surface roughness on impeller blades and hub.

Case ID 3: Diffuser roughness

Only increasing the diffuser surface roughness with a smooth impeller results in Figure 5.4. Compared to the impeller simulation, there is less flow capacity loss at choking conditions. Figure 5.6 shows a higher pressure ratio and efficiency loss but a lower flow capacity loss when increasing surface roughness. The $5.623\,\mu\mathrm{m}$ falls out of line with the other points possibly indicating a simulation inconsistency.

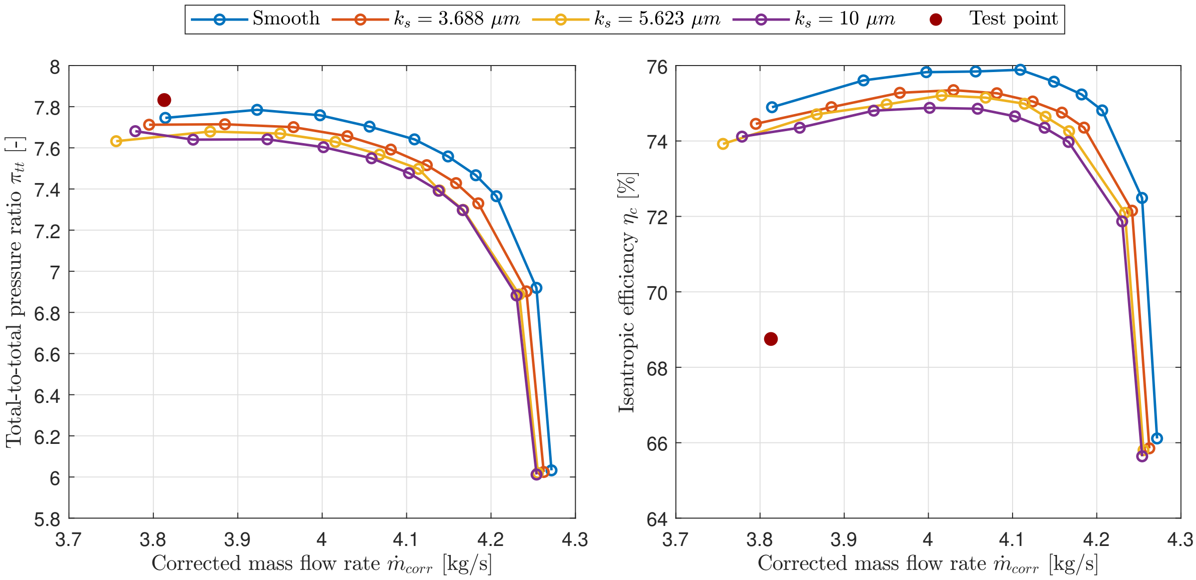

Figure 5.4: Simulated Total-to-total pressure ratio and isentropic compressor efficiency as a function of mass flow rate for increasing surface roughness on diffuser blades and hub.

Roughness comparison

Comparing the same surface roughness of $5.623\,\mu\mathrm{m}$ for the impeller, diffuser or both shows larger losses for the diffuser compared to the impeller with the 2 components together having the highest losses as shown in Figure 5.5. As previously mentioned, the diffuser shows less flow capacity loss at choking conditions as it crosses over the impeller line.

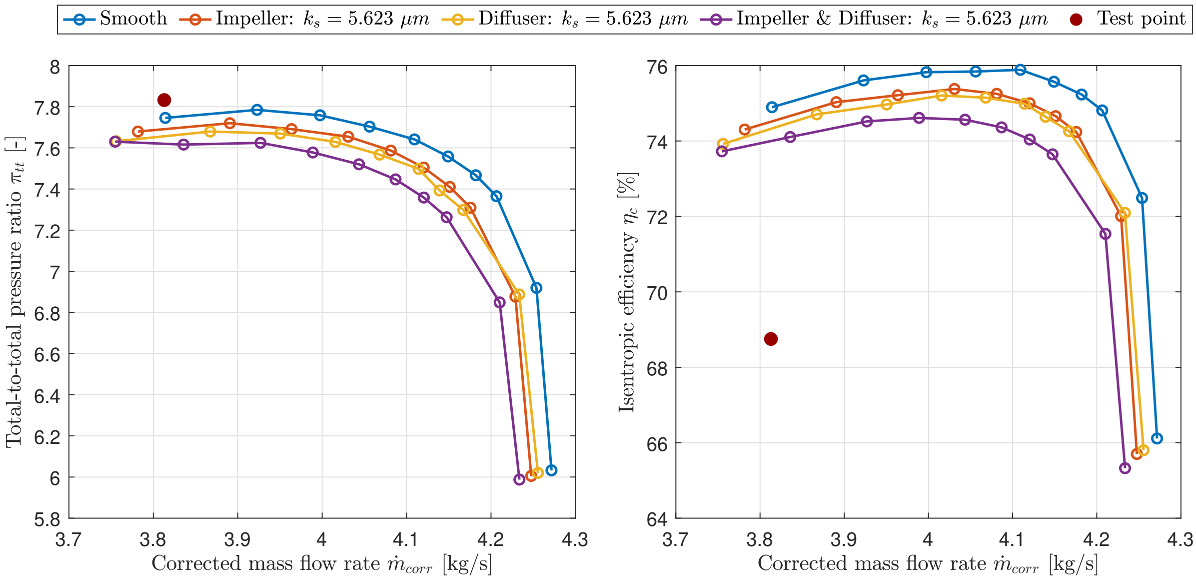

Figure 5.5: Simulated total-to-total pressure ratio and isentropic compressor efficiency as a function of mass flow rate.

Performance and flow capacity sensitivity

Averaging the relative loss in pressure ratio, isentropic efficiency and flow capacity of the different surface roughness conditions compared to the smooth curve results in Figure 5.6. This figure thus indicates the performance sensitivity of the different parts with respect to increasing surface roughness. All 3 simulated parameters show a similar decreasing trend when increasing surface roughness. Increasing surface roughness on the impeller or diffuser shows similar results with the diffuser having a higher loss in pressure ratio and efficiency while the impeller has a higher loss in flow capacity. Adding up the relative losses of the separate impeller and diffuser simulations is indicated by the 'Impeller + Diffuser' line which shows a close match with the impeller & diffuser simulation suggesting that increasing the surface roughness of individual components does not cause additional interaction effects further increasing overall compressor losses. Only the $5.623\,\mu\mathrm{m}$ result shows an increased loss as a result of the diffuser having increased losses at that point resulting in the added up line overshooting the impeller and diffuser simulated together. This possibly indicates an inconsistent CFD result.

Table 5.1 shows the values as used in Figure 5.6 as well as the loss per $\mu\mathrm{m}$ of surface roughness compared to the smooth curve. Apart from the inconsistent $5.623\,\mu\mathrm{m}$ diffuser point, all the considered configurations show reduced losses per $\mu\mathrm{m}$ when increasing surface roughness.

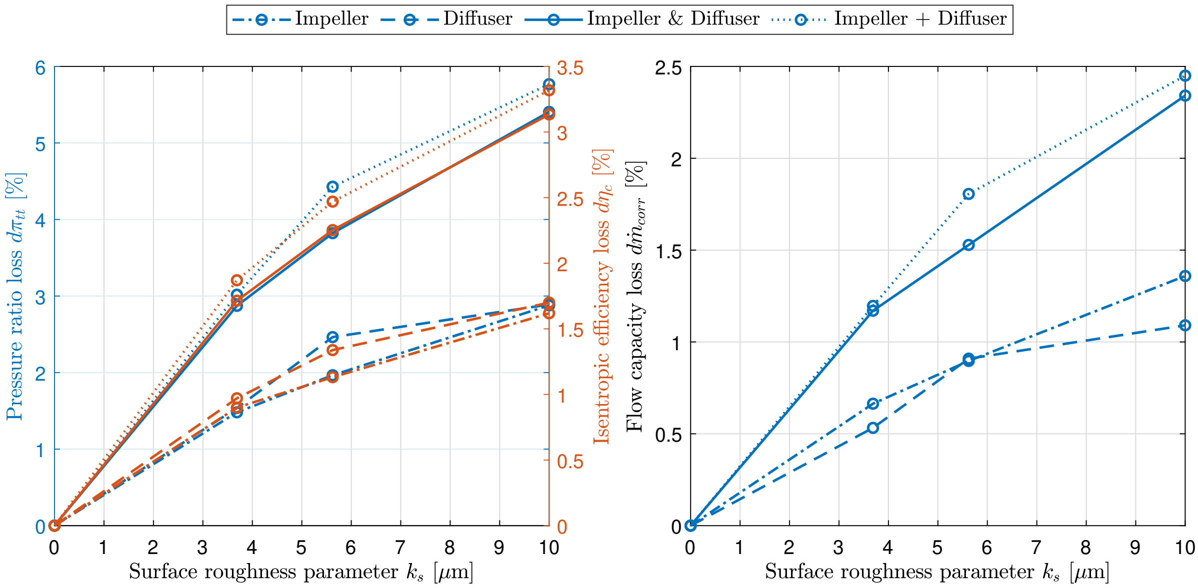

Figure 5.6: Relative loss in pressure ratio, isentropic efficiency and flow capacity as a function of surface roughness parameter k_s.

Case	Metric	Surface roughness [μm]		
		$0 \rightarrow 3.688$	$0 \rightarrow 5.623$	$0 \rightarrow 10$
1: Impeller & diffuser	Pressure ratio loss [%]	2.87	3.82	5.41
	Pressure ratio loss per μm [$\frac{\%}{\mu m}$]	0.78	0.68	0.54
	Efficiency loss [%]	1.72	2.25	3.13
	Efficiency loss per μm [$\frac{\%}{\mu m}$]	0.46	0.40	0.31
	Flow Capacity loss [%]	1.17	1.53	2.34
	Flow Capacity loss per μm [$\frac{\%}{\mu m}$]	0.32	0.27	0.23
2: Impeller	Pressure ratio loss [%]	1.48	1.97	2.88
	Pressure ratio loss per μm [$\frac{\%}{\mu m}$]	0.40	0.35	0.29
	Efficiency loss	0.90	1.13	1.62
	Efficiency loss per μm [$\frac{\%}{\mu m}$]	0.24	0.20	0.16
	Flow Capacity loss [%]	0.66	0.90	1.36
	Flow Capacity loss per μm [$\frac{\%}{\mu m}$]	0.18	0.16	0.14
3: Diffuser	Pressure ratio loss [%]	1.54	2.46	2.89
	Pressure ratio loss per μm [$\frac{\%}{\mu m}$]	0.42	0.44	0.29
	Efficiency loss	0.97	1.34	1.70
	Efficiency loss per μm [$\frac{\%}{\mu m}$]	0.26	0.24	0.17
	Flow Capacity loss [%]	0.53	0.91	1.09
	Flow Capacity loss per μm [$\frac{\%}{\mu m}$]	0.14	0.16	0.11

Table 5.1: Relative loss and relative loss per μm of pressure ratio, isentropic efficiency and flow capacity as a function of surface roughness parameter k_s.

5.1.2. Tip clearance effects

Case ID 4:

Figure 5.7 shows pressure ratio and efficiency of the compressor with base surface roughness $3.688\,\mu\mathrm{m}$ for different tip clearances. Increasing tip clearance reduces pressure ratio, efficiency and flow capacity. Reducing tip clearance gives the opposite result but results in less flow capacity gain in choking conditions. The overall shape of the curves for both increasing and decreasing tip clearance is similar.

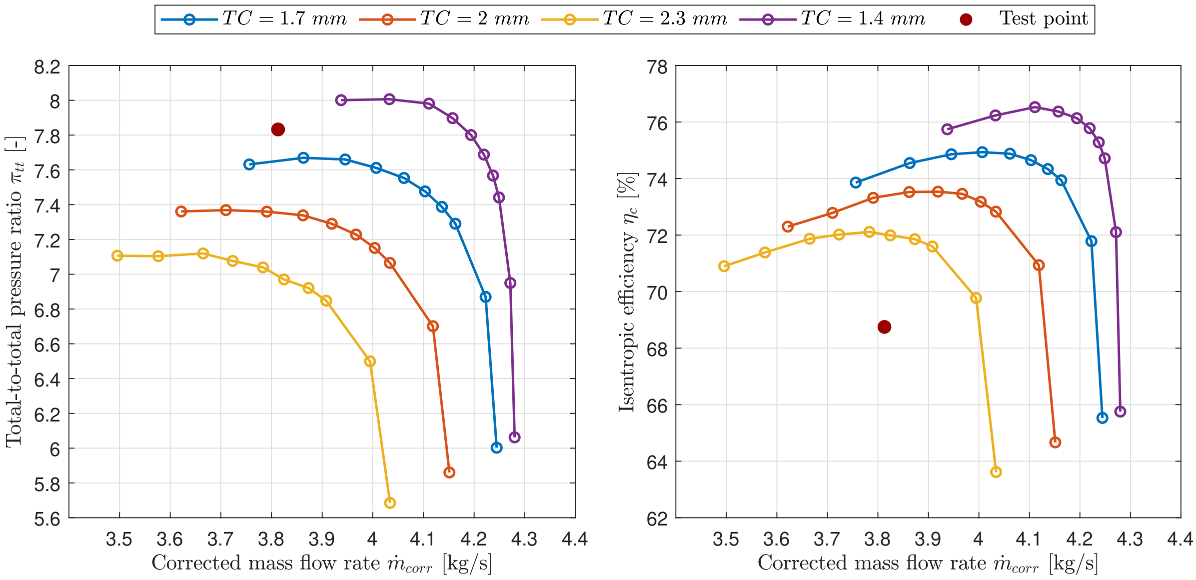

Figure 5.7: Simulated total-to-total pressure ratio and isentropic compressor efficiency as a function of mass flow rate for different impeller tip clearances with surface roughness $3.688\,\mu\mathrm{m}$.

Performance and flow capacity sensitivity

Plotting the performance and flow capacity in terms of tip clearance results in Figure 5.8. Pressure ratio and isentropic efficiency loss show a similar reducing rate of increasing losses with increasing tip clearance while the flow capacity shows an increasing rate of losses as tip clearance increases. Table 5.2 contains the used values as well as the relative loss per $0.1\,\mathrm{mm}$.

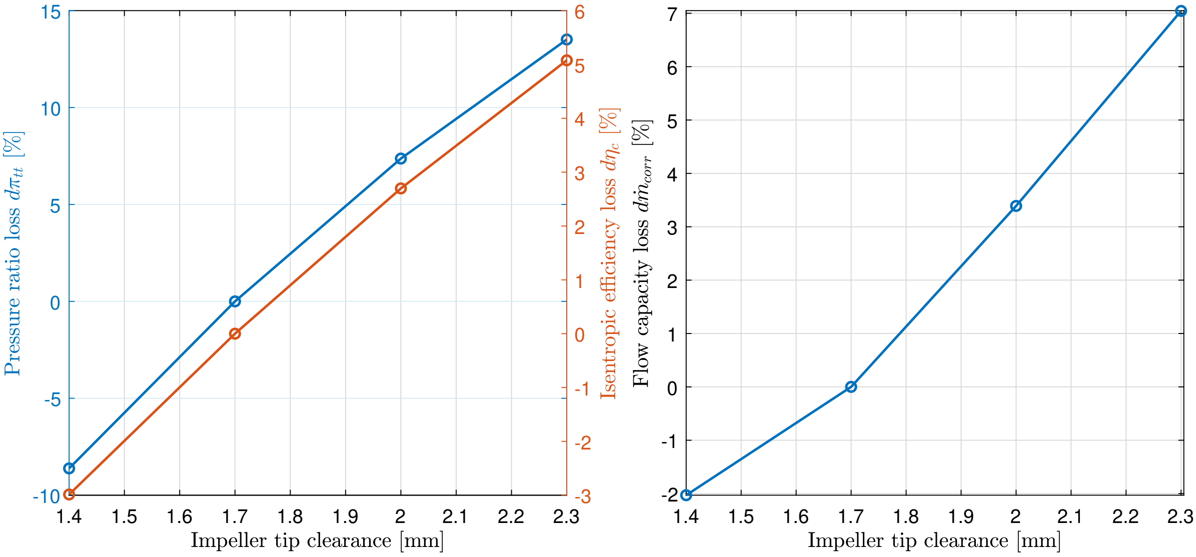

Figure 5.8: Relative loss in pressure ratio, isentropic efficiency and flow capacity as a function of tip clearance.

Case	Metric	Tip clearance [mm]		
		$1.7 \rightarrow 1.4$	$1.7 \rightarrow 2$	$1.7 \rightarrow 2.3$
4: Impeller tip clearance	Pressure ratio loss [%]	-8.62	7.37	13.51
	Pressure ratio loss per $0.1\,\mathrm{mm}$ $[\frac{\%}{0.1mm}]$	-2.87	2.46	2.25
	Efficiency loss [%]	-2.99	2.70	5.08
	Efficiency loss per $0.1\,\mathrm{mm}$ $[\frac{\%}{0.1mm}]$	-1.00	0.90	0.85
	Flow Capacity loss [%]	-2.03	3.39	7.04
	Flow Capacity loss per $0.1\,\mathrm{mm}$ $[\frac{\%}{0.1mm}]$	-0.68	1.13	1.17

Table 5.2: Relative loss and relative loss per $0.1\,\mathrm{mm}$ of pressure ratio, isentropic efficiency and flow capacity as a function of impeller tip clearance.

5.1.3. Surface roughness effects at higher tip clearance

Increasing impeller and diffuser surface roughness at increased tip clearance $2\,\mathrm{mm}$ and $2.3\,\mathrm{mm}$ results in Figures 5.9 and 5.10 respectively. Both show similar results where an increase in surface roughness beyond $5.623\,\mathrm{\mu m}$ does not further reduce pressure ratio and efficiency across the whole curve but does reduce flow capacity.

Case ID 5 & 6:

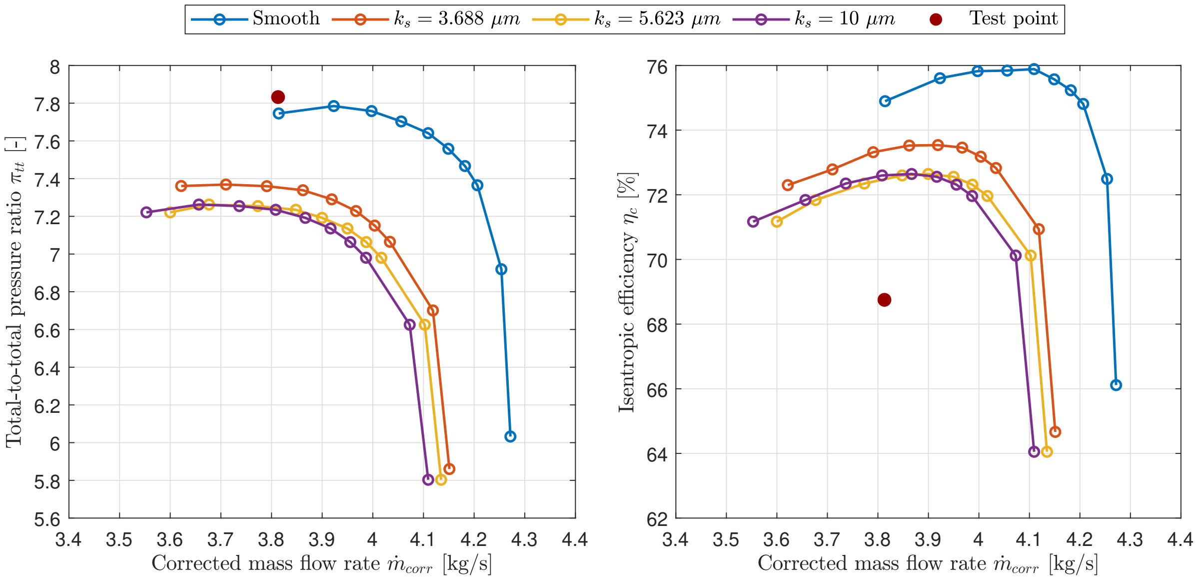

Figure 5.9: Simulated total-to-total pressure ratio and isentropic compressor efficiency as a function of mass flow rate for increasing surface roughness with $2\,\mathrm{mm}$ impeller tip clearance.

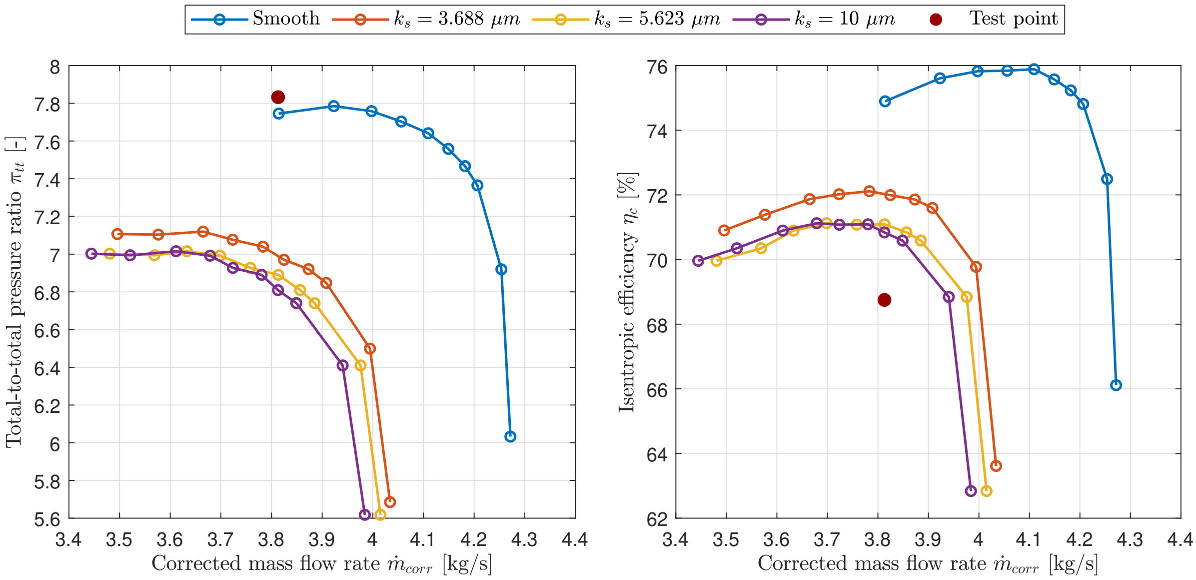

Figure 5.10: Simulated total-to-total pressure ratio and isentropic compressor efficiency as a function of mass flow rate for increasing surface roughness with $2.3\,\mathrm{mm}$ impeller tip clearance.

Performance and flow capacity sensitivity

Figure 5.11 shows the performance and flow capacity loss for the increased impeller tip clearance as well as the earlier results using the nominal $1.7\,\mathrm{mm}$ tip clearance. As the relative difference is always compared to the smooth $1.7\,\mathrm{mm}$ result, there is a large increase in losses from $0\,\mu\mathrm{m}$ to $3.688\,\mu\mathrm{m}$ surface roughness. Table 5.4 contains the relative loss and relative loss values per μm of surface roughness for both $2\,\mathrm{mm}$ and $2.3\,\mathrm{mm}$ tip clearance. Subtracting the relative losses between $10\,\mu\mathrm{m}$ and $3.688\,\mu\mathrm{m}$ of the different tip clearances results in Table 5.3. This table shows that increasing surface roughness at $2\,\mathrm{mm}$ tip clearance shows similar losses compared to increased roughness at the nominal $1.7\,\mathrm{mm}$ tip clearance. Only flow capacity showed additional losses. Further increasing the tip clearance to $2.3\,\mathrm{mm}$ shows increased losses in pressure ratio and efficiency. Flow capacity losses increased in line with the other tip clearance steps.

Tip clearance $[mm]$	1.7	2.0	2.3
Pressure ratio loss difference $[\%]$	2.54	2.38	3.09
Isentropic efficiency loss difference $[\%]$	1.41	1.40	1.94
Flow capacity loss difference $[\%]$	1.17	1.31	1.62

Table 5.3: Difference in relative loss between $10\,\mu\mathrm{m}$ and $3.688\,\mu\mathrm{m}$ roughness for $1.7\,\mathrm{mm}$, $2\,\mathrm{mm}$ and $2.3\,\mathrm{mm}$ tip clearance.

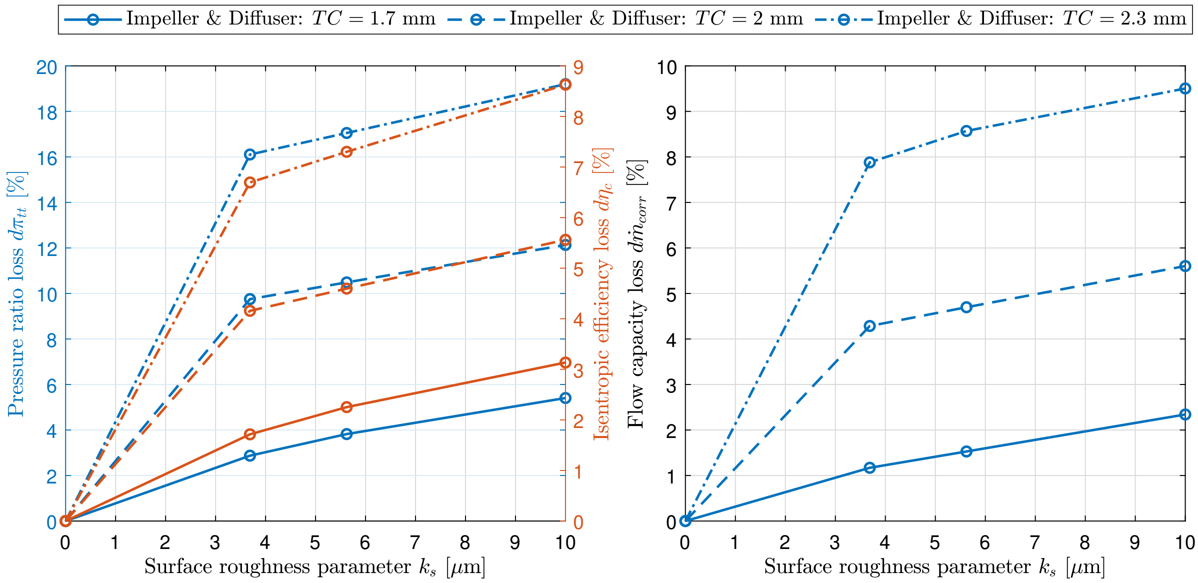

Figure 5.11: Relative loss in pressure ratio, isentropic efficiency and flow capacity as a function of surface roughness parameter k_s for different tip clearances.

Case	Metric	Surface roughness [μm]		
		$0 \rightarrow 3.688$	$0 \rightarrow 5.623$	$0 \rightarrow 10$
5: $2\,\mathrm{mm}$ tip clearance	Pressure ratio loss $[\%]$	9.75	10.49	12.13
	Pressure ratio loss per μm $[\frac{\%}{\mu m}]$	2.64	1.87	1.21
	Efficiency loss $[\%]$	4.16	4.60	5.56
	Efficiency loss per μm $[\frac{\%}{\mu m}]$	1.13	0.82	0.56
	Flow Capacity loss $[\%]$	4.29	4.70	5.60
	Flow Capacity loss per μm $[\frac{\%}{\mu m}]$	1.16	0.84	0.56
6: $2.3\,\mathrm{mm}$ tip clearance	Pressure ratio loss $[\%]$	16.11	17.05	19.20
	Pressure ratio loss per μm $[\frac{\%}{\mu m}]$	4.37	3.03	1.92
	Efficiency loss $[\%]$	6.69	7.30	8.63
	Efficiency loss per μm $[\frac{\%}{\mu m}]$	3.80	2.64	1.67
	Flow Capacity loss $[\%]$	7.88	8.57	9.50
	Flow Capacity loss per μm $[\frac{\%}{\mu m}]$	2.14	1.52	0.95

Table 5.4: Relative loss and relative loss per μm of pressure ratio, isentropic efficiency and flow capacity as a function of surface roughness parameter k_s.

5.2. APU system performance

5.2.1. Surface roughness effects

Using the previously shown performance and flow capacity sensitivities, the average loss in isentropic efficiency and flow capacity is used in GSP to simulate decreasing compressor performance. Figure 5.12 shows the relative increase in fuel flow and EGT when increasing the surface roughness for different tip clearances. Increasing surface roughness at higher tip clearances shows a larger increase in both fuel flow and EGT. The difference in pressure ratio loss between surface roughness $3.688\,\mathrm{μm}$ and $10\,\mathrm{μm}$ at $1.7\,\mathrm{mm}$ is $0.78\,\%$ and $2.50\,\%$ at $2.3\,\mathrm{mm}$.

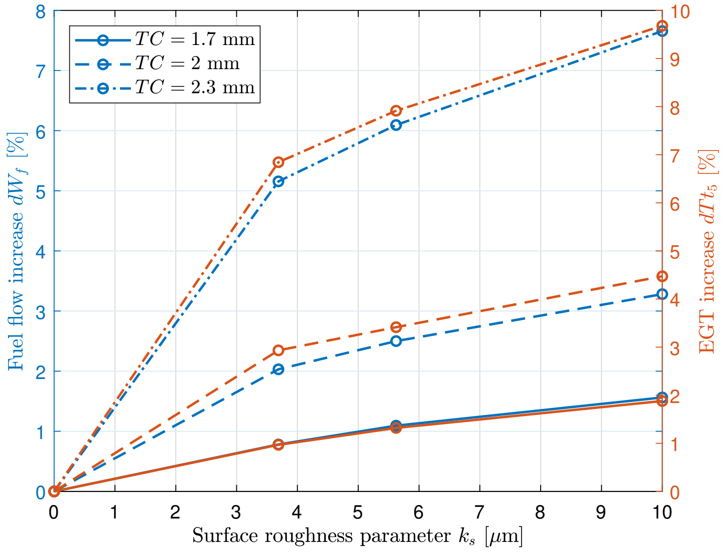

Figure 5.12: Relative fuel flow and EGT increase as a function of surface roughness parameter k_s for different tip clearances.

5.2.2. Tip clearance effects

Evaluating the fuel flow and EGT as a result of tip clearance using the base surface roughness 3.688 µm result in Figure 5.13. The relative increase in fuel flow and EGT increases as tip clearance increases with the initial increase from $1.4\,\mathrm{mm}$ to $1.7\,\mathrm{mm}$ resulting in a $0.78\,\%$ reduction in fuel flow and a $1.12\,\%$ reduction in EGT. Increasing the tip clearance to the maximum $2.3\,\mathrm{mm}$ results in a $4.22\,\%$ increase in fuel flow and a $5.71\,\%$ increase in EGT.

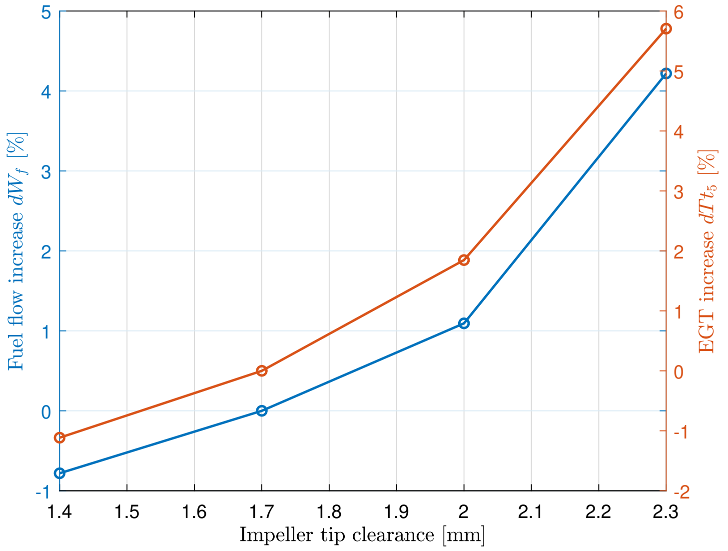

Figure 5.13: Relative fuel flow and EGT difference as a function of impeller tip clearance.

5.2.3. Deterioration map

Simulating the difference in EGT, pressure ratio and fuel flow for 4 steps of efficiency deterioration $d\eta_c$ and flow deterioration $d\dot{m}_{corr}$ results in Figure 5.14. The figure also includes the previously shown results for increasing roughness at $1.7\,\mathrm{mm}$ and $2\,\mathrm{mm}$ tip clearance as shown in case 1 and 5. Figure 5.15 shows the same deterioration map but includes increasing tip clearance at base roughness 3.688 µm.

Increasing efficiency deterioration $d\eta_c$ shows linear increases for the 3 considered variables. Losses in $dEGT$ increase at high flow capacity deterioration with losses in fuel flow reducing slightly. Pressure ratio loss shows a high sensitivity to flow capacity deterioration with sensitivity to efficiency deterioration increasing at higher flow capacity deterioration.

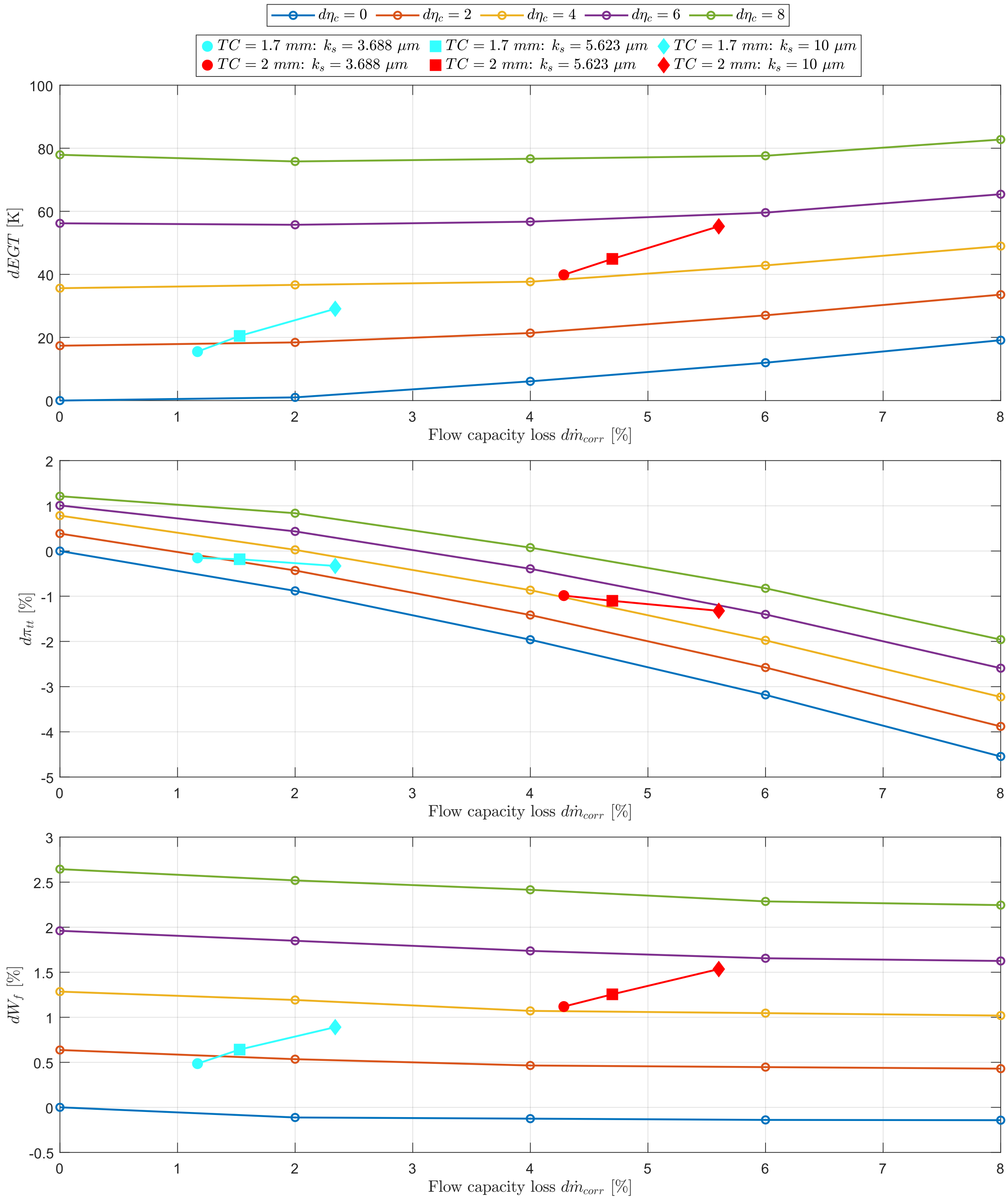

Figure 5.14: Relative difference in EGT, pressure ratio and fuel flow as a function of deterioration in compressor mass flow $d\dot{m}_{corr}$ and efficiency $d\eta_c$ overlaid with different surface roughness as shown in case 1 and 5.

Figure 5.14 shows higher flow capacity deterioration when increasing surface roughness at $2\,\mathrm{mm}$ compared to $1.7\,\mathrm{mm}$. Because of this increased flow capacity deterioration and the upwards trend of the EGT towards these higher values, the $dEGT$ increases more at a higher tip clearance for the same increase in surface roughness. At the same efficiency deterioration, the fuel flow loss slightly reduces when increasing flow capacity deterioration resulting in the relative loss in fuel flow when increasing the surface roughness from $3.688\,\mu\mathrm{m}$ to $10\,\mu\mathrm{m}$ being the same for both $1.7\,\mathrm{mm}$ and $2\,\mathrm{mm}$ tip clearance. Figure 5.15 also shows increasing flow capacity deterioration from $2\,\mathrm{mm}$ to $2.3\,\mathrm{mm}$ compared to going from $1.7\,\mathrm{mm}$ to $2\,\mathrm{mm}$. This results in a higher fuel flow increase and even higher EGT increase as $dEGT$ increases at high flow capacity. The reduction in pressure ratio shows a similar trend with a decrease of $1.32\,\%$ from $2\,\mathrm{mm}$ to $2.3\,\mathrm{mm}$ compared to $0.83\,\%$ from $1.7\,\mathrm{mm}$ to $2\,\mathrm{mm}$.

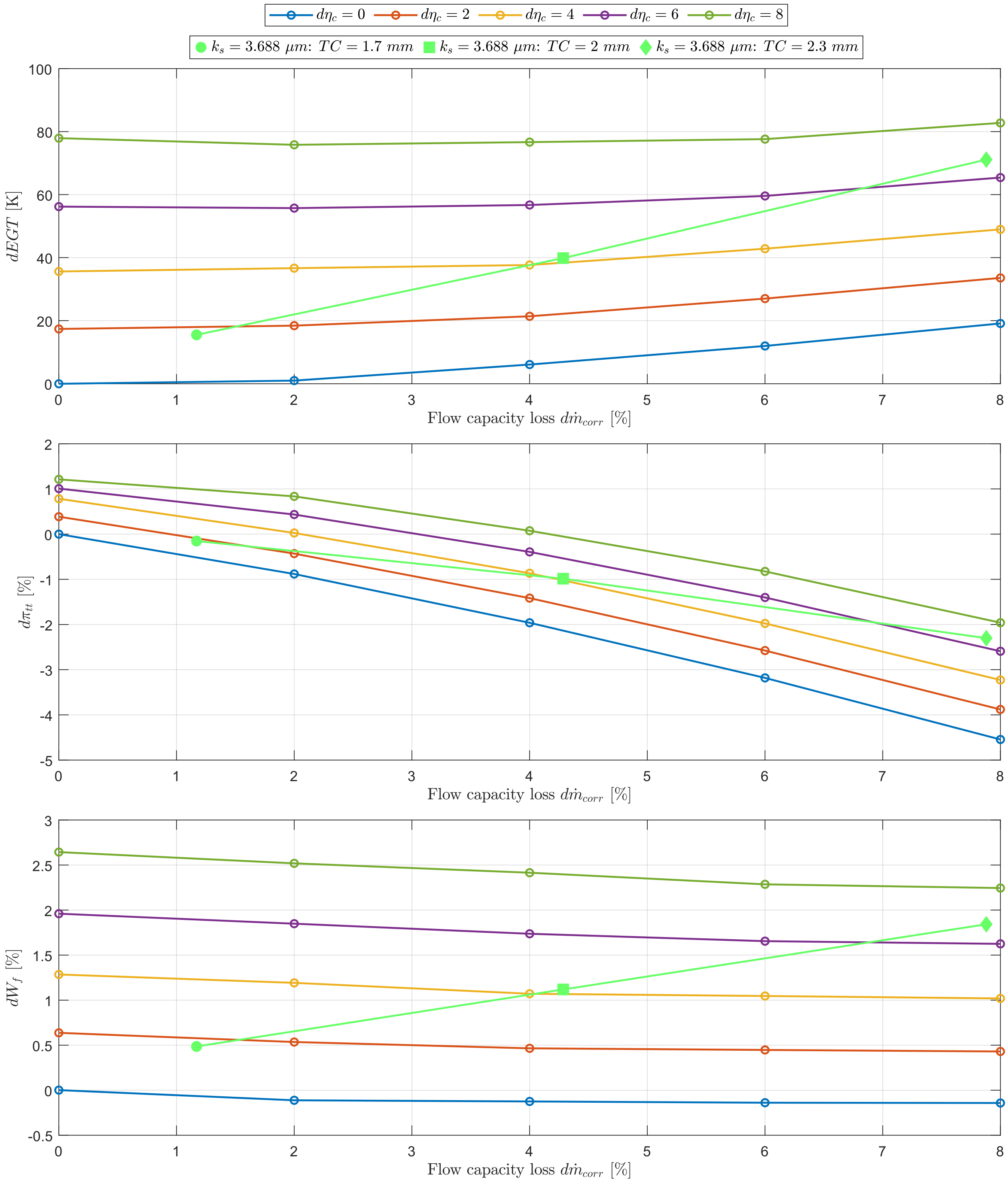

Figure 5.15: Relative difference in EGT, pressure ratio and fuel flow as a function of deterioration in compressor mass flow $d\dot{m}_{corr}$ and efficiency $d\eta_c$ overlaid with increasing tip clearances.

When comparing Table 5.2 with Figure 5.15, it can be seen that there is a discrepancy in the flow capacity and efficiency deterioration values. This is because Table 5.2 shows the relative performance difference of the changing tip clearance with base surface roughness $3.688\,\mu\mathrm{m}$ compared to the nominal tip clearance $1.7\,\mathrm{mm}$ at $3.688\,\mu\mathrm{m}$ while Figure 5.15 shows the relative performance difference compared to nominal tip clearance $1.7\,\mathrm{mm}$ but using a smooth impeller and diffuser. To enable a direct comparison of the effects of changing tip clearance and increasing surface roughness on the same deterioration map, the relative performance difference with respect to the smooth geometries at nominal tip clearance is used for both cases. This means the GSP results of the deterioration map are both compared to the smooth geometries design point parameters of column 2 in Table 4.4. Because of this, the $1.7\,\mathrm{mm}$ value with surface roughness $3.688\,\mu\mathrm{m}$ already shows performance deterioration.

6
Discussion

6.1. Application in maintenance environment

The constructed deterioration map can be used as a decision tool to aid in root cause determination during disassembly. When an APU shows a $40\,\mathrm{K}$ increase in EGT and $1\,\%$ increase in fuel flow the map can be used to indicate an expected tip clearance towards $2.3\,\mathrm{mm}$ assuming the impeller is clean. If the impeller shows a lot of fouling and a rough surface, the same can be done for the surface roughness or even for both tip clearance and surface roughness. When inspecting the compressor, the map can confirm the performance loss avoiding further disassembly of the APU. If the compressor does not show this expected increase in tip clearance and/or surface roughness, the root cause of the performance loss must be in another component of the APU.

In flight condition monitoring includes fuel flow and EGT but does not include compressor pressure ratio limiting the accuracy of the deterioration map in this use case as only 2 of the 3 available relations between the physical compressor deterioration and APU performance can be used. Performing an APU test in a test cell allows a pressure ratio reading increasing the accuracy of the map. For example, if an overhauled APU does not pass the pass-off test after assembly, the map can be used to aid as a decision tool before disassembling the entire APU. If the APU shows an increased EGT of $40\,\mathrm{K}$, pressure ratio loss of $\approx 1\,\%$ and a $\approx 1\,\%$ increase in fuel flow, the compressor stage is expected to show an increased tip clearance of $2\,\mathrm{mm}$ if the surface roughness is the base $3.688\,\mu\mathrm{m}$. Of course, an estimate of different combinations of tip clearance and surface roughness can also be made using the map. If the physical compressor wear aligns with the deterioration map, the compressor stage can be assumed to be the root cause of the APU performance deterioration.

Although the simulations and map are performed for a single model APU, the map is ISA corrected with many APUs having a similar layout, size and performance possibly allowing the map to give an indication for other APU models. If a test is performed and the APU is disassembled, alignment of the compressor stage deterioration with the APU performance loss can be cross checked with the map to validate if the map aligns to that APU model.

6.2. Limitations

The limitations of the performed work are listed below.

- Geometry fidelity: The impeller and diffuser geometries were reconstructed using 3D scans which may not perfectly capture all geometry features. Another limitation is the construction of the BladeGen geometry which is compared visually. Although the geometry looks very similar there will be differences.
- Computational domain: The simulated domain does not include any geometry in front of the impeller as well as the second blade row of the diffuser possibly affecting the pressure recovery and loss distribution.
- Turbulence model: To reduce the mesh size and the needed computational power, the $k-\epsilon$ turbulence model is used instead of the SST turbulence model. As shown in literature and confirmed by the results, the $k-\epsilon$ model is known to overestimate efficiency as a result of underestimated flow separation with the SST turbulence model generally being better for turbomachinery applications.
- CFD validation: Although the model is considered suitable to perform a sensitivity analysis, the correlation between the test point and the CFD simulations can be improved. Only a single test

point is used to validate the simulation with the estimated mass flow rate using assumptions for exhaust gas heat capacity C_{p_5}, fuel lower heating value LHV, generator power factor PF and efficiency η_{gen}.

- Surface roughness measurement: Because of a lack of surface roughness measurement setup, the measured surface roughness was measured locally after which it was applied across the full impeller and diffuser geometries possibly overestimating the surface roughness. Additionally, the surface roughness of the diffuser was not measured separately. Because of the damage to the blades, the measured impeller of the investigated case had a reduced amount of operating hours possibly reducing the impeller fouling and measured surface roughness.
- Sand grain parameter relation: The chosen empirical relation to estimate the sand grain parameter k_s from the measured average surface roughness R_a greatly varies between sources affecting the simulated surface roughness.
- Tip clearance: Since the tip clearance during compressor operation cannot be measured directly, the measured cold tip clearance is used in the simulations. This simulated tip clearance is assumed to be constant along the circumference of the impeller and constant span from hub to shroud. In reality, the tip clearance reduces because of thermal expansion and mechanical deformation while bearing wear can result in non-uniform tip clearance around the circumference of the impeller thus limiting the accuracy of the simulated tip clearance.
- GSP simulation: The constructed model is not a perfect model of the considered APU with many parameters like the combustion efficiency or turbine map being unknown.
- Chosen reference simulation: The relative performance difference for the deterioration map is calculated with respect to a smooth impeller and diffuser, which is not realistic. Increasing the quality of the surface roughness measurement followed by a new reference simulation using realistic surface roughness values for both the the impeller and diffuser could increase the accuracy of the deterioration map as well as the absolute performance values.

7

Conclusion and future work

This thesis set out to determine whether auxiliary power unit performance degradation resulting from compressor deterioration can be simulated using computational fluid dynamics and gas path simulation. Both the impeller and first row of the diffuser are successfully reverse engineered into an Ansys BladeGen model using a 3D scan after which Ansys CFX is used to perform a steady state RANS CFD analysis using a $k - \epsilon$ turbulence model. A grid independence and convergence tolerance analysis is performed after which the CFD model is validated using a pass-off test result from the considered APU.

To evaluate compressor deterioration, changes in impeller tip clearance and/or surface roughness are simulated. Tip clearance is evaluated using increasing and decreasing steps from the nominal cold tip clearance as measured during compressor assembly. Surface roughness is modeled by a sand grain parameter calculated from an average surface roughness value measured using a profilometer. The most important CFD results are summarized in Table 7.1, which shows that:

- Increasing surface roughness on both impeller and diffuser shows reducing increases in losses with increasing roughness.
- Reducing the tip clearance from the nominal value shows a higher efficiency and pressure ratio gain compared to the loss when increasing the tip clearance the same amount. The increase in flow capacity, however, is smaller.
- Increasing tip clearance above the nominal value shows an almost linear increase in pressure ratio loss, efficiency loss, and flow capacity loss.

Case	Metric	Surface roughness [μm]		
		$0 \rightarrow 3.688$	$0 \rightarrow 5.623$	$0 \rightarrow 10$
Surface roughness: impeller & diffuser	Pressure ratio loss [$\%$]	2.87	3.82	5.41
	Pressure ratio loss per μm [$\frac{\%}{\mu m}$]	0.78	0.68	0.54
	Efficiency loss [$\%$]	1.72	2.25	3.13
	Efficiency loss per μm [$\frac{\%}{\mu m}$]	0.46	0.40	0.31
	Flow Capacity loss [$\%$]	1.17	1.53	2.34
	Flow Capacity loss per μm [$\frac{\%}{\mu m}$]	0.32	0.27	0.23
Case	Metric	Tip clearance [mm]		
		$1.7 \rightarrow 1.4$	$1.7 \rightarrow 2$	$1.7 \rightarrow 2.3$
Impeller tip clearance	Pressure ratio loss [$\%$]	-8.62	7.37	13.51
	Pressure ratio loss per $0.1\,\mathrm{mm}$ [$\frac{\%}{mm}$]	-2.87	2.46	2.25
	Efficiency loss [$\%$]	-2.99	2.70	5.08
	Efficiency loss per $0.1\,\mathrm{mm}$ [$\frac{\%}{mm}$]	-1.00	0.90	0.85
	Flow Capacity loss [$\%$]	-2.03	3.39	7.04
	Flow Capacity loss per $0.1\,\mathrm{mm}$ [$\frac{\%}{mm}$]	-0.68	1.13	1.17

Table 7.1: Relative loss and relative loss per μm and mm of pressure ratio, isentropic efficiency and flow capacity as a function of surface roughness parameter k_s and tip clearance resulting from compressor CFD simulations.

The results demonstrated that both surface roughness and tip clearance impact compressor efficiency, pressure ratio and flow capacity. Using these deteriorated compressor data, the impact on APU system performance is simulated using gas turbine simulation program GSP. A summary of the results is shown in Table 7.2 where increasing surface roughness shows a reducing increase in losses. Reducing tip clearance shows a lower fuel flow decrease, EGT decrease and pressure ratio gain compared to the losses when increasing tip clearance the same amount. Increasing tip clearance another step showed a further increase in fuel flow, EGT and pressure ratio loss indicating a stronger sensitivity when tip clearance increases.

Case	Metric	Surface roughness [μm]		
		$0 \rightarrow 3.688$	$0 \rightarrow 5.623$	$0 \rightarrow 10$
Surface roughness: impeller & diffuser	Fuel flow increase [%]	0.78	1.09	1.56
	EGT increase [%]	0.97	1.32	1.88
	Pressure ratio loss [%]	0.28	0.36	0.58
Case	Metric	Tip clearance [mm]		
		$1.7 \rightarrow 1.4$	$1.7 \rightarrow 2$	$1.7 \rightarrow 2.3$
Impeller tip clearance	Fuel flow increase [%]	-0.78	1.09	4.22
	EGT increase [%]	-1.12	1.85	5.71
	Pressure ratio loss [%]	-0.50	1.09	2.39

Table 7.2: Relative fuel flow increase, EGT increase and pressure ratio loss as a function of surface roughness parameter k_s and tip clearance resulting from GSP system simulations.

An ISA-corrected deterioration map visualizes the increases in EGT, pressure ratio and fuel flow for a range of compressor efficiency deterioration and flow deterioration. Overlaying this with the compressor efficiency and flow capacity deterioration caused by surface roughness and tip clearance, a relation between physical compressor wear and APU system performance is made allowing the map to serve as a decision tool to identify whether the compressor is the source of performance loss within the APU.

Although the absolute accuracy of the results is limited by assumptions in geometry reconstruction, turbulence modeling, and validation data, the study provides an indication of the relative reduction in APU system performance and demonstrates a working proof of concept in the form of a deterioration. Therefore, it is concluded that compressor CFD with gas turbine simulation offers a viable approach to assess compressor deterioration effects and their impact on APU performance, thus enhancing APU condition monitoring and supporting root cause determination in a maintenance environment.

7.1. Research questions

Main Question:

Can APU performance degradation as a result of compressor deterioration be estimated using compressor CFD simulation with reverse engineered compressor geometries?

Yes, 3D scanned impeller and diffuser geometries are reverse engineered into an Ansys BladeGen model and meshed using Ansys TurboGrid. A steady RANS CFD simulation is performed using Ansys CFX to estimate the performance deterioration as a function of tip clearance and surface roughness. The compressor CFD analysis is used to construct a compressor map which is implemented into a GSP gas turbine model. Losses in compressor efficiency and flow capacity are used to evaluate APU system performance in terms of fuel flow, EGT and compressor pressure ratio producing a deterioration map of the APU performance due to compressor deterioration. Although absolute accuracy of the result is limited, the relative performance reduction is estimated successfully.

Sub-questions:

- *How can the impeller and diffuser geometry of a centrifugal compressor be reverse engineered to be used in CFD simulation?*
  A high fidelity 3D scan is reduced using Rhino 3D to reduce the file size. After manually removing floating elements and closing the mesh holes it is converted to a surface after which it is be imported to Ansys DesignModeler. An Ansys BladeGen model is created and overlaid with the

3D scanned surface mesh in Ansys DesignModeler so they can easily be compared. Using Ansys Workbench to manage the BladeGen model allows it to automatically update in DesignModeler enabling quick changes and visual comparison. When the BladeGen model is completed it is be fed into TurboGrid to start meshing.

- *What are the main deterioration mechanisms in an APU centrifugal compressor and what are the corresponding damage effects?*
  It is concluded that the main deterioration mechanisms are rubbing, fouling, particle ingestion, and erosion. Particle ingestion and erosion increase surface roughness and may cause cutting and pitting of the impeller blades. Rubbing occurs when the impeller blades contact the shroud mainly leading to impeller damage and an increase in tip clearance. Fouling results in contaminants sticking to the compressor flow surfaces increasing surface roughness and potentially changing the shape of the surfaces to a smaller degree.
- *How can these damage effects and resulting performance loss be simulated in CFD simulations?*
  Ansys TurboGrid allows setting a tip clearance during the meshing process. In this thesis, the tip clearance is assumed to be constant span along the impeller radius. The surface roughness can be applied to flow surfaces in Ansys CFX using a sand grain parameter k_s. This variable is calculated using an empirical relation including an average surface roughness measurement R_a. There is a wide variation in empirical relations reported across sources, with no clear consensus. This leads to a large variety in the possible surface roughness k_s.
- *Can the compressor CFD simulation with reverse engineered geometries be validated using an APU test cell result?*
  The mass flow rate of the test result is calculated using an energy balance with assumptions for C_p, fuel LHV, generator efficiency and power factor resulting in limited accuracy. The simulated pressure ratio matches the test result while the efficiency is overestimated because of the $k - \epsilon$ turbulence model. Since the aim of this thesis is to evaluate relative performance differences, the simulation is considered to match the test result sufficiently.
- *Can the performance reduction of an APU with a degraded compressor be simulated?*
  Yes, a GSP model is used to evaluate the APU system performance. This is done using a constructed compressor map made from a simulated speed line. Keeping the operating conditions and shaft power the same with the corrected speed N_c equal to 1, the difference in fuel flow, pressure ratio and EGT is evaluated.

7.2. Future work

With more available CPU power, the accuracy of CFD compressor model can be increased by using an SST turbulence model with a finer mesh. This would likely result in better efficiency alignment compared to the test result. The second row of the compressor diffuser could also be reverse engineered and included in the simulation domain.

Similar to the work in this thesis, the turbine side of the APU can also be characterized after which the constructed GSP model can be improved to increase accuracy of the simulated performance parameters.

If alignment of the compressor deterioration map with a certain model APU is deemed insufficient, the workflow of this thesis could be improved to construct a similar model in a short time frame allowing different maps for different APU models to be created.

Bibliography

[1] Maj Rudolph C Schulte. “Design Analysis of BMW 003 Turbojet”. In: *Aviation Magazine* 45 (1946), pp. 55–68.

[2] American Institute of Aeronautics and Astronautics. *Case Study in Aircraft Design: The Boeing 727*. AIAA Case Study. American Institute of Aeronautics & Astronautics, 1978. ISBN: 9781563472770. URL: `https://books.google.be/books?id=uJRTAAAAMAAJ`.

[3] Dieter Scholz. “An optional APU for passenger aircraft”. In: *5th Council of European Aerospace Societies Air and Space Conference: Challenges in European Aerospace, Delft*. 2015.

[4] Umair Ahmed, Fakhre Ali, and Ian Jennions. “A review of aircraft auxiliary power unit faults, diagnostics and acoustic measurements”. In: *Progress in Aerospace Sciences* 124 (2021), p. 100721. ISSN: 0376-0421. DOI: `https://doi.org/10.1016/j.paerosci.2021.100721`. URL: `https://www.sciencedirect.com/science/article/pii/S0376042121000269`.

[5] AN Startsev et al. “Multi-disciplinary design of high-speed compressors for prospective turboshaft engine”. In: *30th Congress of the International Council of the Aeronautical Sciences, ICAS 2016*. 2016.

[6] J. P. Bons. “A Review of Surface Roughness Effects in Gas Turbines”. In: *Journal of Turbomachinery* 132.2 (Jan. 2010), p. 021004. ISSN: 0889-504X. DOI: `10.1115/1.3066315`. eprint: `https://asmedigitalcollection.asme.org/turbomachinery/article-pdf/132/2/021004/5754570/021004\_1.pdf`. URL: `https://doi.org/10.1115/1.3066315`.

[7] A Ghenaiet, RL Elder, and SC Tan. “Particles trajectories through an axial fan and performance degradation due to sand ingestion”. In: *Turbo Expo: Power for Land, Sea, and Air*. Vol. 78507. American Society of Mechanical Engineers. 2001, V001T03A079.

[8] Awatef A Hamed et al. “Turbine blade surface deterioration by erosion”. In: (2005).

[9] H Hefazi, K Kaups, and R Murry. “Ice accretion on a radial inflow turbine blade”. In: (1996).

[10] Gbanaibolou Jombo et al. “Influence of Fouling on Compressor Dynamics: Experimental and Modeling Approach”. In: *Journal of Engineering for Gas Turbines and Power* 140.3 (Oct. 2017), p. 032603. ISSN: 0742-4795. DOI: `10.1115/1.4037913`. eprint: `https://asmedigitalcollection.asme.org/gasturbinespower/article-pdf/140/3/032603/6178274/gtp\_140\_03\_032603.pdf`. URL: `https://doi.org/10.1115/1.4037913`.

[11] M.D.Paramour and P.G. Jennings. “Operational Requirements for Helicopter Engines for U.K. services.” In: *Propulsion and Energetics Panel on Technology Requirements for Small Gas Turbineso* 82nd Symposium (1993).

[12] R. Kurz and K. Brun. “Degradation in Gas Turbine Systems”. In: *Journal of Engineering for Gas Turbines and Power* 123.1 (Nov. 2000), pp. 70–77. ISSN: 0742-4795. DOI: `10.1115/1.1340629`. eprint: `https://asmedigitalcollection.asme.org/gasturbinespower/article-pdf/123/1/70/5746793/70\_1.pdf`. URL: `https://doi.org/10.1115/1.1340629`.

[13] P.K.Harris. “Erosion in centrifugal compressor impellers”. PhD thesis. Cranfield University, 1996.

[14] M. Fathy Hussein and W. Tabakoff. “Computation and plotting of solid particle flow in rotating cascades”. In: *Computers & Fluids* 2.1 (1974), pp. 1–15. ISSN: 0045-7930. DOI: `https://doi.org/10.1016/0045-7930(74)90002-4`. URL: `https://www.sciencedirect.com/science/article/pii/0045793074900024`.

[15] Adel Ghenaiet. “Turbomachinery performance degradation due to erosion effect”. PhD thesis. Sept. 2001.

[16] W Tabakoff. “Turbomachinery performance deterioration exposed to solid particulates environment”. In: (1984).

[17] W. Tabakoff. “Study of single-stage axial flow compressor performance deterioration”. In: *Wear* 119.1 (1987), pp. 51–61. ISSN: 0043-1648. DOI: `https://doi.org/10.1016/0043-1648(87)90097-4`. URL: `https://www.sciencedirect.com/science/article/pii/0043164887900974`.

[18] W. Walsh, Karen Thole, and Chris Joe. “Effects of Sand Ingestion on the Blockage of Film-Cooling Holes”. In: Jan. 2006. DOI: `10.1115/GT2006-90067`.

[19] Cyrus B Meher-Homji and Andrew Bromley. “Gas Turbine Axial Compressor Fouling And Washing.” In: (2004).

[20] Ihor S Diakunchak. “Performance deterioration in industrial gas turbines”. In: *Journal of Engineering for Gas Turbines and Power;(United States)* 114.2 (1992).

[21] Uyioghosa Igie et al. “Industrial Gas Turbine Performance: Compressor Fouling and On-Line Washing”. In: *Journal of Turbomachinery* 136.10 (June 2014), p. 101001. ISSN: 0889-504X. DOI: `10.1115/1.4027747`. eprint: `https://asmedigitalcollection.asme.org/turbomachinery/article-pdf/136/10/101001/6300280/turbo\_136\_10\_101001.pdf`. URL: `https://doi.org/10.1115/1.4027747`.

[22] Gali Musa et al. “Gas Turbine Compressor Washing Economics and Optimization Using Genetic Algorithm”. In: *Journal of Engineering for Gas Turbines and Power* 144.9 (Aug. 2022), p. 091012. ISSN: 0742-4795. DOI: `10.1115/1.4055187`. eprint: `https://asmedigitalcollection.asme.org/gasturbinespower/article-pdf/144/9/091012/6911406/gtp\_144\_09\_091012.pdf`. URL: `https://doi.org/10.1115/1.4055187`.

[23] *Investigation Into the Effect of Tip Clearance on Centrifugal Compressor Performance*. Vol. Volume 1: Turbomachinery. Turbo Expo. June 1988, V001T01A066. DOI: `10.1115/88-GT-190`. eprint: `https://asmedigitalcollection.asme.org/GT/proceedings-pdf/GT1988/79184/V001T01A066/4456891/v001t01a066-88-gt-190.pdf`. URL: `https://doi.org/10.1115/88-GT-190`.

[24] Changhee Kim et al. “Study on the performance of a centrifugal compressor considering running tip clearance”. In: *International Journal of Refrigeration* 65 (2016), pp. 92–102. ISSN: 0140-7007. DOI: `https://doi.org/10.1016/j.ijrefrig.2015.11.008`. URL: `https://www.sciencedirect.com/science/article/pii/S0140700715003709`.

[25] Carl Pfleiderer. *Die Kreiselpumpen für Flüssigkeiten und Gase: Wasserpumpen, Ventilatoren, Turbogebläse Turbokompressoren*. Springer-Verlag, 2013.

[26] B Eckert. *u. E. SCHNELL: Axial-und Radialkompressoren*. 1961.

[27] Y. Senoo and M. Ishida. “Deterioration of Compressor Performance Due to Tip Clearance of Centrifugal Impellers”. In: *Journal of Turbomachinery* 109.1 (Jan. 1987), pp. 55–61. ISSN: 0889-504X. DOI: `10.1115/1.3262070`. eprint: `https://asmedigitalcollection.asme.org/turbomachinery/article-pdf/109/1/55/5838725/55\_1.pdf`. URL: `https://doi.org/10.1115/1.3262070`.

[28] Y. Senoo and M. Ishida. “Pressure Loss Due to the Tip Clearance of Impeller Blades in Centrifugal and Axial Blowers”. In: *Journal of Engineering for Gas Turbines and Power* 108.1 (Jan. 1986), pp. 32–37. ISSN: 0742-4795. DOI: `10.1115/1.3239882`. eprint: `https://asmedigitalcollection.asme.org/gasturbinespower/article-pdf/108/1/32/5567319/32\_1.pdf`. URL: `https://doi.org/10.1115/1.3239882`.

[29] Teemu Turunen-Saaresti and Ahti Jaatinen. “Influence of the Different Design Parameters to the Centrifugal Compressor Tip Clearance Loss”. In: *Journal of Turbomachinery* 135.1 (Oct. 2012), p. 011017. ISSN: 0889-504X. DOI: `10.1115/1.4006388`. eprint: `https://asmedigitalcollection.asme.org/turbomachinery/article-pdf/135/1/011017/6294015/turb\_135\_1\_011017.pdf`. URL: `https://doi.org/10.1115/1.4006388`.

[30] G. Eisenlohr and H. Chladek. “Thermal Tip Clearance Control for Centrifugal Compressor of an APU Engine”. In: *Journal of Turbomachinery* 116.4 (Oct. 1994), pp. 629–634. ISSN: 0889-504X. DOI: `10.1115/1.2929453`. eprint: `https://asmedigitalcollection.asme.org/turbomachinery/article-pdf/116/4/629/5940524/629\_1.pdf`. URL: `https://doi.org/10.1115/1.2929453`.

[31] Mohammadreza Kadivar, David Tormey, and Gerard McGranaghan. “A review on turbulent flow over rough surfaces: Fundamentals and theories”. In: *International Journal of Thermofluids* 10 (2021), p. 100077. ISSN: 2666-2027. DOI: `https://doi.org/10.1016/j.ijft.2021.100077`. URL: `https://www.sciencedirect.com/science/article/pii/S266620272100015X`.

[32] F. J. Wiesner. “A New Appraisal of Reynolds Number Effects on Centrifugal Compressor Performance”. In: *Journal of Engineering for Power* 101.3 (July 1979), pp. 384–392. ISSN: 0022-0825. DOI: `10.1115/1.3446586`. eprint: `https://asmedigitalcollection.asme.org/gasturbinespower/article-pdf/101/3/384/5886062/384\_1.pdf`. URL: `https://doi.org/10.1115/1.3446586`.

[33] H. Simon and A. Bu¨lska¨mper. “On the Evaluation of Reynolds Number and Relative Surface Roughness Effects on Centrifugal Compressor Performance Based on Systematic Experimental Investigations”. In: *Journal of Engineering for Gas Turbines and Power* 106.2 (Apr. 1984), pp. 489–498. ISSN: 0742-4795. DOI: `10.1115/1.3239592`. eprint: `https://asmedigitalcollection.asme.org/gasturbinespower/article-pdf/106/2/489/5676932/489\_1.pdf`. URL: `https://doi.org/10.1115/1.3239592`.

[34] *Sensitivity Study on the Impact of Surface Roughness Due to Milling on the Efficiency of Shrouded Centrifugal Compressor Impellers*. Vol. Volume 6: Turbomachinery, Parts A and B. Turbo Expo. May 2006, pp. 1069–1076. DOI: `10.1115/GT2006-90499`. eprint: `https://asmedigitalcollection.asme.org/GT/proceedings-pdf/GT2006/4241X/1069/4533082/1069\_1.pdf`. URL: `https://doi.org/10.1115/GT2006-90499`.

[35] K. L. Suder et al. “The Effect of Adding Roughness and Thickness to a Transonic Axial Compressor Rotor”. In: *Journal of Turbomachinery* 117.4 (Oct. 1995), pp. 491–505. ISSN: 0889-504X. DOI: `10.1115/1.2836561`. eprint: `https://asmedigitalcollection.asme.org/turbomachinery/article-pdf/117/4/491/5840349/491\_1.pdf`. URL: `https://doi.org/10.1115/1.2836561`.

[36] Awatef Hamed, W. Tabakoff, and D. Singh. “Modeling of Compressor Performance Deterioration Due to Erosion”. In: *International Journal of Rotating Machinery* 4 (Jan. 1998). DOI: `10.1155/S1023621X98000207`.

[37] R Numakura, T Kawakubo, and H Tamaki. “Prediction of surface roughness effects on centrifugal compressor performance”. In: *Turbomach Soc Jpn* 37 (2009), pp. 554–558.

[38] Nicholas Cumpsty and Andrew Heyes. *Jet propulsion*. Cambridge University Press, 2015.

[39] Runa Nivea Pinto et al. “Computational fluid dynamics in turbomachinery: a review of state of the art”. In: *Archives of Computational Methods in Engineering* 24.3 (2017), pp. 467–479.

[40] P.G. Tucker. “Trends in turbomachinery turbulence treatments”. In: *Progress in Aerospace Sciences* 63 (2013), pp. 1–32. ISSN: 0376-0421. DOI: `https://doi.org/10.1016/j.paerosci.2013.06.001`. URL: `https://www.sciencedirect.com/science/article/pii/S0376042113000547`.

[41] Lee Gibson et al. “Assessment of turbulence model predictions for a centrifugal compressor simulation”. In: *Journal of the Global Power and Propulsion Society* 1 (July 2017), p. 2II890. DOI: `10.22261/2II890`.

[42] Robert S Rogallo and Parviz Moin. “Numerical simulation of turbulent flows”. In: *Annual review of fluid mechanics* 16 (1984), pp. 99–137.

[43] Haecheon Choi and Parviz Moin. “Grid-point requirements for large eddy simulation: Chapman’s estimates revisited”. In: *Physics of Fluids* 24.1 (Jan. 2012), p. 011702. ISSN: 1070-6631. DOI: `10.1063/1.3676783`. eprint: `https://pubs.aip.org/aip/pof/article-pdf/doi/10.1063/1.3676783/14069693/011702\_1\_online.pdf`. URL: `https://doi.org/10.1063/1.3676783`.

[44] James Tyacke et al. “Turbomachinery simulation challenges and the future”. In: *Progress in Aerospace Sciences* 110 (2019), p. 100554. ISSN: 0376-0421. DOI: `https://doi.org/10.1016/j.paerosci.2019.100554`. URL: `https://www.sciencedirect.com/science/article/pii/S0376042119300715`.

[45] A. K. SLEITI and J. S. KAPAT. “Comparison between EVM and RSM turbulence models in predicting flow and heat transfer in rib-roughened channels”. In: *Journal of Turbulence* 7 (2006), N29. DOI: `10.1080/14685240500499343`. eprint: `https://doi.org/10.1080/14685240500499343`. URL: `https://doi.org/10.1080/14685240500499343`.

[46] Wei SUN. “Assessment of advanced RANS turbulence models for prediction of complex flows in compressors”. In: *Chinese Journal of Aeronautics* 36.9 (2023), pp. 162–177. ISSN: 1000-9361. DOI: `https://doi.org/10.1016/j.cja.2023.06.007`. URL: `https://www.sciencedirect.com/science/article/pii/S1000936123001930`.

[47] Ansys Inc. *Best Practice: RANS Turbulence Modeling in Ansys CFD*. Accessed: 2025-06-20. Ansys Inc. 2023. URL: `https://www.ansys.com/resource-library/best-practices/rans-turbulence-modeling-in-ansys-cfd`.

[48] Philippe Spalart and Steven Allmaras. “A One-Equation Turbulence Model for Aerodynamic Flows”. In: *AIAA* 439 (Jan. 1992). DOI: `10.2514/6.1992-439`.

[49] Jose Moreno et al. “Deficiencies in the Spalart–Allmaras Turbulence Model for the Prediction of the Stability Boundary in Highly Loaded Compressors”. In: *Journal of Turbomachinery* 142.12 (Dec. 2020), p. 121012. ISSN: 0889-504X. DOI: `10.1115/1.4047784`. eprint: `https://asmedigitalcollection.asme.org/turbomachinery/article-pdf/142/12/121012/6598097/turbo\_142\_12\_121012.pdf`. URL: `https://doi.org/10.1115/1.4047784`.

[50] SimScale GmbH. *k–Omega SST Model*. Accessed: 2025-06-20. 2024. URL: `https://www.simscale.com/docs/simulation-setup/global-settings/k-omega-sst/`.

[51] Ernesto Casartelli et al. “Application of Advanced RANS Turbulence Models for the Prediction of Turbomachinery Flows”. In: *Journal of Turbomachinery* 144.1 (Sept. 2021), p. 011008. ISSN: 0889-504X. DOI: `10.1115/1.4051938`. eprint: `https://asmedigitalcollection.asme.org/turbomachinery/article-pdf/144/1/011008/6756132/turbo\_144\_1\_011008.pdf`. URL: `https://doi.org/10.1115/1.4051938`.

[52] F. R. Menter. “Two-Equation Eddy-Viscosity Turbulence Models for Engineering Applications”. In: *AIAA Journal* 32.8 (1994), pp. 1598–1605. DOI: `10.2514/3.12149`.

[53] ANSYS Inc. *ANSYS TurboGrid, Release 2024 R2*. Licensed commercial software. ANSYS Inc. Canonsburg, PA, USA, 2024.

[54] CFD Online. *Dimensionless Wall Distance (y□)*. Accessed: 2025-06-24. 2013. URL: `https://www.cfd-online.com/Wiki/Dimensionless_wall_distance_(y_plus)`.

[55] Jousef Murad. *What is y^+ (yplus)?* Accessed: 2025-06-25. SimScale Community Forum. May 2018. URL: `https://www.simscale.com/forum/t/what-is-y-yplus/82394`.

[56] Fluid Mechanics 101 Aidan Wimshurst. *[CFD] What are Wall Functions and How do they work?* 2019.

[57] Frank M. White. *Fluid Mechanics*. 7th ed. New York: McGraw-Hill Education, 2011. ISBN: 9780073529349.

[58] Philip P Walsh and Paul Fletcher. *Gas turbine performance*. John Wiley & Sons, 2004.

[59] Randall C. Boehm et al. “Lower heating value of jet fuel from hydrocarbon class concentration data and thermo-chemical reference data: An uncertainty quantification”. In: *Fuel* 311 (2022), p. 122542. ISSN: 0016-2361. DOI: `https://doi.org/10.1016/j.fuel.2021.122542`. URL: `https://www.sciencedirect.com/science/article/pii/S001623612102411X`.

[60] Bonnie J McBride and Sanford Gordon. *Computer Program for Calculation of Complex Chemical Equilibrium Compositions and Applications II. Users Manual and Program Description: Users Manual and Program Description-2*. Tech. rep. 1996.

[61] Abdulrahman Abdullah Bahashwan et al. “The Lean Blowout Prediction Techniques in Lean Premixed Gas Turbine: An Overview”. In: *Energies* 15.22 (2022). ISSN: 1996-1073. DOI: `10.3390/en15228343`. URL: `https://www.mdpi.com/1996-1073/15/22/8343`.

[62] Vyankatesh R Wakharkar and RB Buktar. “Reverse Engineering of Pump Casing and Impeller”. In: (2016).

[63] C. C. Koch and L. H. Smith. “Loss Sources and Magnitudes in Axial-Flow Compressors”. In: *Journal of Engineering for Power* 98.3 (June 1976), pp. 411–424. DOI: `10.1115/1.3446202`.

[64] Thomas Adams, Christopher Grant, and Heather Watson. “A simple algorithm to relate measured surface roughness to equivalent sand-grain roughness”. In: *International Journal of Mechanical Engineering and Mechatronics* 1.2 (2012), pp. 66–71.

[65] *Measurements and Predictions of Surface Roughness Effects on the Turbine Vane Aerodynamics*. Vol. Volume 6: Turbo Expo 2003, Parts A and B. Turbo Expo. June 2003, pp. 291–303. DOI: `10.1115/GT2003-38580`. eprint: `https://asmedigitalcollection.asme.org/GT/proceedings-pdf/GT2003/36894/291/4550198/291\_1.pdf`. URL: `https://doi.org/10.1115/GT2003-38580`.

[66] Mohit Biglarian et al. “Prediction of erosive wear locations in centrifugal compressor using CFD simulation and comparison with experimental model”. In: *Journal of the Brazilian Society of Mechanical Sciences and Engineering* 41 (Feb. 2019). DOI: `10.1007/s40430-019-1610-5`.

[67] Adel Ghenaiet. “Simulation of Particle Trajectories and Erosion in a Centrifugal Compressor”. In: *Journal of Turbomachinery* 134.5 (May 2012), p. 051022. ISSN: 0889-504X. DOI: `10.1115/1.4004448`. eprint: `https://asmedigitalcollection.asme.org/turbomachinery/article-pdf/134/5/051022/5851284/051022\_1.pdf`. URL: `https://doi.org/10.1115/1.4004448`.

[68] Lee Gibson et al. “Assessment of turbulence model predictions for a centrifugal compressor simulation”. In: *Journal of the Global Power and Propulsion Society* 1 (2017), pp. 142–156. DOI: `10.22261/2II890`. URL: `https://doi.org/10.22261/2II890`.